國 立 交 通 大 學
光電工程學系碩士班

碩士論文

有機無機電晶體應用於氣體感測之研究

Organic and Inorganic Transistors for Gas Sensing

研究生：余治寬

指導教授：冉曉雯 教授

蔡娟娟 教授

中 華 民 國 一 百零一 年 七 月

有機無機電晶體應用於氣體感測之研究

Organic and Inorganic Transistors for Gas Sensing

研 究 生：余治寬　　Student：Chih-Kuan Yu

指導教授：冉曉雯 教授　　Advisor：Prof. Hsiao-Wen Zan

蔡娟娟 教授　　Prof. Chuang-Chuang Tsai

國 立 交 通 大 學

光電工程學系碩士班

碩 士 論 文

A Thesis

Submitted to Institute of Electro-Optical Engineering

College of Electrical Engineering and Computer Science

National Chiao Tung University

in Partial Fulfillment of the Requirements

for the Degree of Master

in

Electro-Optical Engineering

July 2012

Hsinchu, Taiwan, Republic of China

中華民國一百零一年七月

有機無機電晶體應用於氣體感測之研究

研究生：余治寬　　指導教授：冉曉雯 教授

蔡娟娟 教授

國立交通大學光電工程學系碩士班

摘要

在本研究中，我們首先將介紹一個有機垂直通道空間電荷限制電晶體的氣體感測器。透過具備氧化或還原特性的氣體對電晶體的主動層造成電子摻雜或電子解摻雜的效應，進而改變垂直通道中的電位分佈，導致輸出電流密度的改變。藉由對於氨氣具備 30 ppb 的感測極限，此氣體感測器將可以應用在被非侵入式呼氣監控的定點照護檢驗。

此外，一個無機非晶銦鎵鋅氧化物薄膜電晶體混合式氣體感測器也將被介紹。我們將金屬氧化物半導體覆蓋在電晶體的背通道上面，作為氣體感測層以及第二個閘極。透過接觸具備氧化或還原特性的氣體分子，電荷將會在感測層和氣體分子間傳遞，造成感測層的位能改變，使得第二個閘極的電位改變，導致輸出電流改變。此無機混合式氣體感測器對於氨氣和一氧化氮的感測極限分別為 50 ppb 和 3ppm。

最後，我們將在附錄中介紹提升非晶銦鎵鋅氧化物薄膜電晶體載子遷移率的初步結果。透過使用飛秒雷射照射非晶銦鎵鋅氧化物薄膜表面，我們可以得到一個高載子遷移率(~84 cm^2/Vs)的電晶體。其可能原因為，飛秒雷射照射非晶銦鎵鋅氧化物薄膜後，會造成通道導電率的提升，進而使得載子遷移率提升。

Organic and Inorganic Transistors for Gas Sensing

Student : Chih-Kuan Yu Advisor: Prof. Hsiao-Wen Zan

Prof. Chuang-Chuang Tsai

Department of Electro-Optical Engineering

National Chiao Tung University

Abstract

In this thesis, we report a very sensitive gas sensor embedded in a vertical polymer space-charge-limited transistor at first. The oxidizing and reducing gases act as electron dedoping and electron doping agents on the transistor active layer to change the potential distribution in the vertical channel and hence to change the output current density. With a 30-ppb detection limit to ammonia, the sensor can be used for non-invasive breath monitor in point-of-care applications.

In addition, a metal-oxide sensing layer is capped onto an amorphous indium gallium zinc oxide (a-IGZO) thin-film transistor (TFT) to form a hybrid sensor. The metal-oxide layer, served as a second gate, forms a *p*-*n* junction with a-IGZO film. Oxidizing or reducing vapor molecules act like electron acceptors or electron donors to change the potential of the metal-oxide layer and the current of a-IGZO TFT. A sensitive response to 50 ppb ammonia and 3 ppm nitric oxide is obtained.

In the end, a preliminary result of femtosecond laser irradiation (FLI) on a-IGZO TFTs is demonstrated in appendix. A high mobility (~84 cm^2/Vs) top-gate (TG) a-IGZO TFT is proposed. It is supposed that FLI on a-IGZO film induces an increase in channel conductivity and forms a high field-effect mobility (~84 cm^2/Vs) TG a-IGZO TFT.

誌謝

時光匆匆，碩班生活就這樣結束了。不同於一般的碩士生，我選擇了五年學碩這一條路，這是一條生活非常充的路。在別人眼裡悠哉的大四這年，身兼大四生和碩一生的我，背負著二十四個碩班學分和修學完的專選學分。為了能夠再碩二能全心做實驗，兩大二生沒有兩樣。回首過去的二十三年，非常感謝我的爸媽無私的照顧。還記得在那腸胃炎，發燒，及打球扭傷的時刻，老爸老媽總是及時的伸出援手。此外，在經濟上全力的支持，讓我不用為了吃和生活去打工，可以全心投入學業。對於老爸和老媽，我有說不完的感謝和感激。

打從專題研究開始，冉老師的細心指導以及不離不棄，讓我感到格外的溫暖和感激。在這和冉老師相處的兩年半時光裡，很慶幸沒有讓老師為了我而大動肝火。非常感謝老師在研究上的指導和建議，沒有這兩年的磨練，或許就不會有今天比較有耐心，比較細心，和比較有點專業知識的我。此外我也要感謝孟老師和洪老師的適時指導。

感謝每一位學長姐，同學和學弟妹真誠的對待。在我們實驗室裡，我沒有感受到別人傳言中的研究所的冷淡和自私，相反的卻是慢慢的人情味。或許大家的實驗都很忙碌，但是在需要幫忙時總是可以找到幫助。首先我想感謝銘志學長從專題生到現在不時的建議和幫助，讓我在最無助的時候找到方向。感謝長紘一起度過大半的碩二生活，如果沒有你的陪伴、幫忙和建議，我的碩班生涯應該會是悲慘世界。感謝所有幫我量過膜厚的大家：浩文、宇帆、郁茜、俊閔、永軒、和郁馨。感謝良豪和峻宏，換檔板、清腔和蝕刻如果沒有你們的互相照應，這些日子應該會是很難熬。感謝電晶體、Sensor、LED、IGZO、Solar 組以的各位以及助理們。最後，要特別感謝洪銓！謝謝你在我碩二的後半段回歸做 IGZO 時，陪伴幫忙量測以及接下採購量測機台的工作，辛苦你了加油！

碩班的這些日子裡，做過 Sensor，SCLT solar cell，SCLT sensor，和 IGZO TFT ，可以說除了 LED 以外，其他各組的東西都摸索過一點皮毛。真的很感謝有機實驗室的各位，讓我度過如此充時的日子。很開心有你們作伴，畢業快樂。 治寬 2012 年 7 月

Contents

Figures Captions

Tables Captions

Chapter 1 Introduction

1.1 Organic Semiconductor Materials

Organic material has wildly been used in electronic devices due to advantages of low cost, light weight, solution-processed, and the compatibility to flexible applications. Organic materials are mainly composed of carbon, hydrogen, and oxygen atoms. The basic chemical structure of molecules is called monomer. In general, polymers consist of 10^5~10^6 monomers. The so-called conductive polymers refer to the conjugated polymer. The conductive mechanism of conjugated polymers is utilizing the delocalized orbital so that electrons cannot be bound in a single atom and can move in orbital. In other words, there are unsaturated bonding on carbon atoms in the main chain of conjugated polymer resulting in a main chain with alternating single and double bonds. The conjugated condition of alternating single and double bonds is called conjugated bonding. Polyacetylene (PA) is a common conjugated polymers as shown in Fig.1-1. There are conductive mechanisms of conjugated polymer including intrachain move and interchain move. Polyacetylene as example, there are four valence electrons of carbon of which three valence electrons form the coplanar sp^2 orbital and one valence electron forms the P_z orbital perpendicular to the sp^2orbital. In the formed coplanar sp^2 orbital, two valance electrons forms σ bonding with adjacent two carbons and one bonds with hydrogen. The formed P_z orbital will overlap with P_z orbital electron cloud of adjacent carbon atom and forms delocalized π bonding. Because the low energy levels of σ

bonding are fulfilled, ionization energy is large. As a result, σ bonding in main chain dominates the mechanical properties of polymer. Besides, the delocalized π bonding makes electrons easily move in the long chain of polymer which is called intrachain move. When there is multiple molecules stack, electrons can also move through orbitals of adjacent molecules by the overlapped electron clouds. In this situation, it is called interchain move.

We will introduce materials as hole transport layer and the insulator layer as follows.

1.1.1 Hole Transport Material – Poly(3-hexylthiophene)

In organic materials, the hole mobility (μ_h) is higher than the electron mobility (μ_e) [1]. Therefore, high hole mobility(μ_h) organic materials is chosen as the active layer.

Poly(3-hexylthiophene) (P3HT) is a hole-transporting organic semiconductor. As shown in Fig. 1-2(a), the main chain of P3HT is thiophene and the side chain is hexyl. There are three types of the connections between main chain and side chain: head to tail (HT), head to head (HH) and tail to tail (TT) as shown in Fig. 1-2(b) [1]. There are two common P3HT, regionregular-P3HT (rr-P3HT) and regionrandom-P3HT (rd-P3HT). The difference between them is the ratio of HT to HH. For rr-P3HT, ratio of HT to HH is about 66:1, while the ratio is 1:1 for rd-P3HT. The higher proportion of HT side chain in P3HT, the greater mobility in field effect transistor (FET) [2,3]. The rr-P3HT which we use is purchased from Sigma Aldrich Chemical Cooperation. The average molecular weight is 87000, melting point is 238℃, the HT ratio is higher than 98.5% and LUMO/HOMO equals to 3.0/5.2.

As the formation of P3HT film, it tends to self assemble and forms a 2-dimentional planar conjugated structure. The way that P3HT packs is affected by surface of substrate and annealing condition. As shown in Fig. 1-3, there are two stacking directions, π-π stacking and alkyl stacking. In general, the alkyl chains will impede charge transport so that mobility in this direction is the lower. On the other hand, the partial overlap of adjacent π-orbitals will enhance the mobility [4]. Because of the anisotropic of mobility, it is common that plane-on stacking is expected for vertical channel devices and edge-on stacking is expected in horizontal channel devices. Therefore, for our vertical space charge limited transistor (SCLT), plane-on stacking is expected.

1.1.2 Insulator Layer – Poly(4-vinylphenol)

Poly(4-vinylphenol) (PVP) has melting point at about 360℃ and average molecule weight 25000. To prevent the damage of the insulator property of PVP during fabrication processes, poly(melamine-co-formaldehyde) methylated (PMF, average weight = 511) is added, and cross-link is formed after annealing . Fig. 1-4 shows the chemical structure of PVP and PMF.

1.2 Vertical Organic Semiconductors

In general, the reduction of channel length in horizontal transistors needs photolithography which will increase the cost. Therefore, transistors with vertical channel can reduce channel length without expensive photolithography. Space-charge-limited transistor

(SCLT) demonstrated here has vertical channel and is not field effect transistor. The channel length is the thickness of the organic layer. Like Static-Induction Transistor (SIT), another vertical channel transistor, there are some advantages such as high output current, low operation voltage, high work frequency and high output on/off ratio [5]. Current of SCLT is controlled by space-charge-limited current (SCLC) like vacuum tube triode.

Metal-insulator-metal (MIM) diode is a simple way to test semiconductor characteristics for not only insulator but organic material. Through the MIM diode, we can check control of leakage current, polymer morphology and carrier injection ability.

1.3 Application of Metal Oxide Semiconductor for Sensing

Recently, metal oxide semiconductors, such as SnO_2, WO_x, ZnO, MoO_3, and TiO_2, have been widely used in detection of toxic gases [6-9]. Toxic gases such as NO_x, NH_3, CO, H_2S and SO_x do harm to the environmental and human health. The sensing mechanism is utilizing the change in conductivity of metal oxide semiconductors. When the metal oxides is exposed to the toxic gases, reduction or oxidation reactions occurs at the surface of metal oxides and changes the conductivity of it [10,11]. Among the metal oxide semiconductors, tungsten oxide, as a n-type semiconductors, is considered as a promising material for toxic gases detection [12,13].

1.4 Metal Oxide Semiconductor Thin Film Transistors

Metal oxide semiconductor is considered as a promising candidate for next generation thin film transistors [14]. Application of metal oxide TFTs on active-matrix organic light-emitting diode displays (AMOLEDs) has attract much attention in recent years. Particularly, high performance of amorphous In-Ga-Zn oxide (a-IGZO) as active layer of TFTs exhibited a high mobility (>10 cm^2/Vs) and a good sub-threshold swing (S.S.) (0.2 V/decade) in a-IGZO TFTs [15,16]. In addition, a-IGZO TFTs have advantages such as the capability of low process temperature, high transparency in visible light region (λ = 400 nm~700 nm), high uniformity over large area, and large band gap (>3 eV) resulting in insensitivity to natural light [17]. Besides, the carrier concentration of a-IGZO film is controllable by modulating the ratio of argon to oxygen, power, and operating pressure during sputter. The a-IGZO film can be deposited by radio-frequency sputter which enables to deposit thin films of high-melting-temperature materials over large areas at low substrate temperatures [18]. However, H. Hosono *et al.* proposed that the chemical species and/or a structure in a thin film are unstable when thin films are deposited at low temperatures [18,19]. Oppositely, they are stable while thin films are deposited at high temperatures. The chemical species and/or a structure are frozen in the as-deposited thin film which relax to a more stable state and give the atoms more energy to rearrange upon thermal annealing, leading to an appreciable change in the electron transport properties [18,19]. Most oxide TFTs especially

a-IGZO TFTs, are fabricated using physical vapor deposition (PVD) technique at room temperature and often require a high temperature (>300℃) post-deposition thermal annealing process to get high-performance and high-stability TFTs [18-24]. Among the post-deposition thermal annealing techniques, rapid thermal annealing (RTA) or furnace annealing are usually utilized to anneal the metal-oxide TFT devices [22,23,24]. For the application of a-IGZO TFTs on the flexible substrate, high temperature thermal annealing may damage the substrates. Development of the low annealing temperature technique is necessary for flexible substrates and other temperature-limited substrates.

1.5 Motivation

1.5.1 Space Charge Limited Transistor (SCLT) Sensor

Organic semiconductor materials (OSMs) have been investigated and applied to thin-film transistors because of the low-cost and large-area fabrication on flexible substrates [25]. The gas-sensing ability of OSMs is an unique property that allows the integration of vapor sensors with organic thin-film transistors (OTFTs), which has been extensively studied recently [26,27]. However, high operation voltage (> 10 V) is usually required in these OTFT-based gas sensor. Sensitivity may be limited because the gas molecules mostly contact with bulk area (the exposing area) rather than channel area (buried under bulk region) [28,29]. In this work, we propose a gas sensor based on a vertical polymer transistor. The current flows in the bulk region of the vertical channel. Exposing the vertical channel to gas molecules creates a significant

interaction between channel and gas molecules and hence a high gas sensitivity. The high sensitivity to ammonia enables the development of non-invasive breath ammonia analysis for monitoring dysfunction of the human body [30]. For such applications, a portable and real-time ammonia sensor with a detection limit of 50 ppb is critical, but is still challenging [30]. Our results may facilitate the development of low-cost point-of-care technology.

1.5.2 Amorphous IGZO TFT Hybrid Sensor

Basing on the aforementioned sensing application of metal oxide semiconductor, our a-IGZO TFT hybrid sensor combines the advantages of high mobility (>10 cm^2/Vs) of a-IGZO TFT and the gas sensing ability of tungsten oxide ($W_{18}O_{49}$ in here). We expect the sensing response can be enhanced by the high performance a-IGZO TFT. Tungsten oxide as sensing layer is capped on the back channel of conventional bottom-gate top-contact a-IGZO TFT. The capping layer is served as a floating second gate to influence of the characteristics of a-IGZO TFT [31].

Figures of Chapter 1

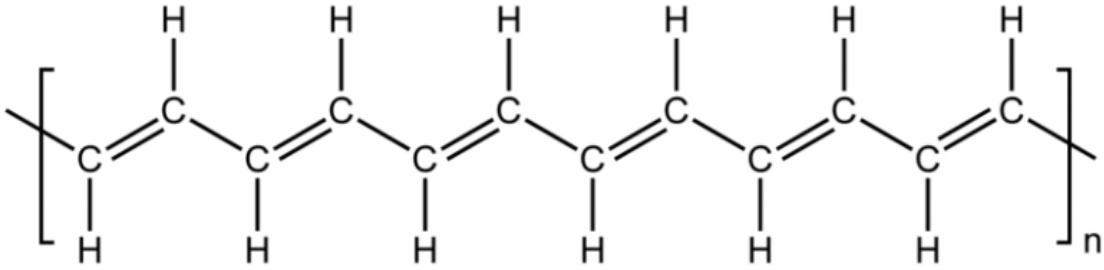

Fig. 1-1 Chemical structure polyacetylene (PA).

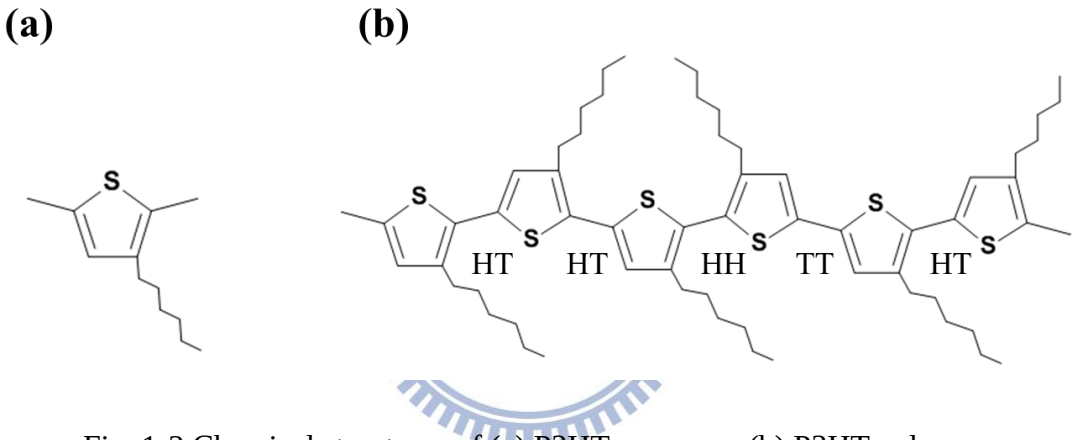

Fig. 1-2 Chemical structures of (a) P3HT monomer (b) P3HT polymer

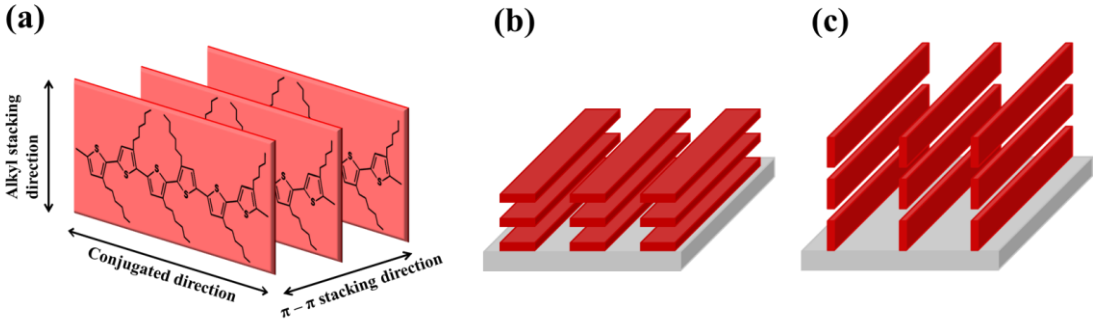

Fig. 1-3 (a) The Schematic diagram of P3HT conjugation direction, π-π stacking direction and alkyl stacking direction (b) Plane-on stacking of P3HT. (c) Edge-on stacking of P3HT.

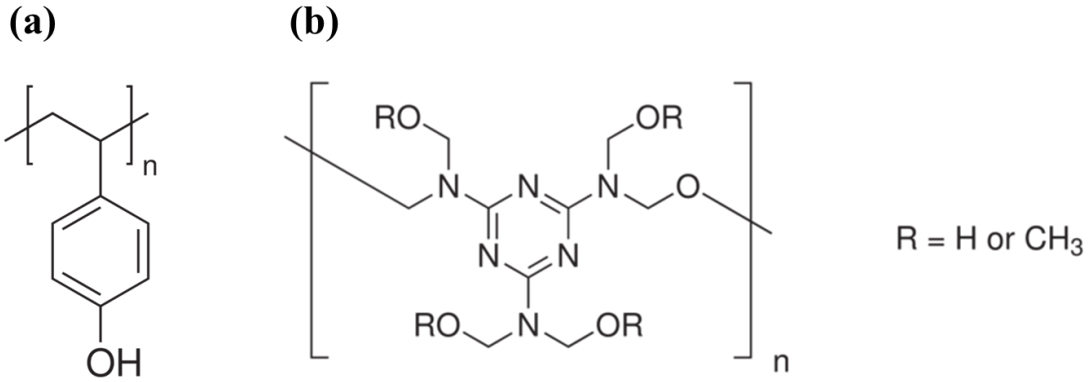

Fig. 1-4 Chemical structures of PVP and PMF. (a) PVP and (b) PMF.

Chapter 2 Theoretical Background

2.1 Metal-Semiconductor Junction

Because of the different work functions of metal and semiconductor, two kinds of contact are formed in the junction between metal and semiconductor interface. One is ohmic contact and the other is schottky contact. The characteristics of current as a function of voltage are shown in Fig. 2-1.

Take p-type semiconductor as example. When fermi-level (E_f) of metal is higher than that of p-type semiconductor, indicating the work function of metal (Φm) is smaller than that of p-type semiconductor (Φs). In thermal equilibrium, fermi-levels of both metal and semiconductor are equal. To satisfy the continuity of vacuum energy (Eo), the energy band of p-type semiconductor near junction should bend downward and forms a energy barrier. When the additional forward bias voltage is applied on p-type semiconductor, the energy barrier would decrease. As the applied forward voltage is large enough to overcome the energy barrier, holes in semiconductor can transport to metal resulting in the increase of current. Oppositely, the additional reverse bias voltage applied on semiconductor increases the energy barrier which allows only little leakage current. In this case, the junction of metal and semiconductor is called Schottky contact as shown in Fig. 2-2. On the other hand, when the Fermi-level of metal is lower than Fermi-level of p-type semiconductor, work function of metal is larger than that of p-type semiconductor (Φm>Φs). Ideally, there is no energy barrier

in the junction of metal and semiconductor.Therefore, despite applying forward or reverse bias voltage, the current is proportional to voltage and follows the Ohm's law. As a result, this situation is called ohmic contact as shown in Fig. 2-3.

The issue of the junction between organic materials and metal has been discussed for decades. There are dipoles generated in the junction resulting in band bending. The phenomenon of band bending can be reduced by using different organic materials. However, there is still not a complete theorem to explain problems of the energy band between metals and organic materials including small molecules and conjugated polymers. The band theorem of inorganic semiconductors can be adopted to explain organic semiconductors. However, in inorganic semiconductor, the electron affinity and ionic potential determine the conduction band and valence band respectively, while, in organic semiconductors, lowest unoccupied molecular orbital (LUMO) and highest occupied molecular orbital (HOMO) are used. Furthermore, one organic semiconductor regarded as whether electron donor or electron acceptor is depending on the distribution of LUMO and HOMO.

2.2 Charge Transportation of Organic Conjugated Polymer

As aforementioned, there isn't a complete theory to demonstrate the carrier transportation in conjugated polymers. In general, theories in electrical characteristics can be separated to bulk limited and contact limited.

2.2.1 Bulk Limited and Space Charge Limited Current Theories.

Bulk limited theory can be explained by space charge limited current. The space charge limited current (SCLC) theory states the phenomenon that the current is controlled by the semiconductor itself and there is no contact limited to affect the injection of carriers. For adopting SCLC theory, the junction of metal and semiconductor should be ohmic contact, or the junction barrier should be smaller than 0.2 eV due to the continuous increase of additional bias.

The behavior of SCLC is found in the insulator by Rose and Lampert originally. They also proved the Power-Law which states the current is proportional to voltage squared ($I \sim V^2$). The so-called SCLC indicates, in the devices, the injection rate of carriers is faster than the transportation rate of carriers and the injected carriers would accumulate in semiconductor forming space charges. The accumulated carriers then produce a built-in electric field to prohibit carrier injection and reach a dynamic equilibrium. As a result, the SCLC refers to the current dominated by space charges accumulated in organic semiconductor. This phenomenon often occurs in materials with low carrier mobility. Therefore, organic materials are mostly explained by SCLC theory. Actually, accumulation of carriers is a bad phenomenon in light-emitting devices and solar cells. In light-emitting devices, carriers inject from electrode to light-emitting layer. If the carrier-injecting rate is faster than carrier-transporting rate in light-emitting layer, carriers would accumulate in the interface of electrode and light-emitting

layer resulting in the decrease of efficiency. Besides, in solar cells, if carrier-dissociating rate is so fast that carriers accumulate in dissociation region, it would also decrease the efficiency.

In general, the transporting length in organic material layer is longer than that in space charge region. The diffusion current due to the difference of carrier concentration is negligible. As a result only the drift current induced by electric field is considered. Under the circumstance that there is no traps in semiconductor, for a single carrier transportation, the current density and thickness (L) of devices follow Mott-Gurney square law [32]. The following equation shows the relationship between current density and thickness where ε is dielectric constant of semiconductor, L is thickness (or drift space between electrodes), V is applied voltage across electrodes and μ_{eff} is effective carrier mobility (μ_{eff} is a function of electric and temperature. In small electric field and fixed temperature, it can be regarded as a constant.)

$$J = \frac{9}{8} \varepsilon \mu_{eff} \frac{V^2}{L^3}$$

2.2.2 Thermionic Emission Theory and Tunneling Effect

The injecting amount of carriers suffers from junction limitation when the energy barrier is larger than 0.3 eV. There are two theories to explain the phenomenon. One is thermionic emission theory as the additional bias voltage is smaller than flat band voltage; the other is tunneling effect as the additional bias voltage overcomes the turn-on voltage.

(1) Thermionic emission theory

Thermionic emission theory states that carriers can overcome the energy barrier between metal and organic semiconductor to transport due to the energy barrier between metal and organic semiconductor is small enough or the additional bias voltage is small than the flat-band voltage. The thermionic emission equation is as follows.

$$J = J_{ST} \left[exp \left(\frac{eV}{kT} \right) - 1 \right]$$

And

$$J_{ST} = A^* \times T^2 exp\left(\frac{-e\phi_B}{kT} \right), \quad A^* \equiv \frac{4\pi e m^* k^2}{h^3}$$

A* is Richardson constant, ϕ_B is the height of junction energy barrier, k is Boltzmann constant and T is absolute temperature.

From above equations, we can find that $J_{ST} \sim T^2$, indicating temperature has a great impact on thermionic emission. Fig. 2-4 shows the schematic diagram of thermionic emission theory.

(2) Tunneling effect

If the energy barrier near the junction of metal and semiconductor is too high, carriers can hardly across the barriers. However, when the additional bias voltage is greater than flat band voltage and reaches the conductive voltage, energy band of semiconductor layer can therefore bend. As we can know, band width of energy barrier is proportional to band height of energy barrier and inversely proportional to additional electric field. Therefore, by this

property, we can reduce the band width so that carriers can tunnel through the barrier and enter semiconductor layer as shown in Fig. 2-5. In tunneling effect, there isn't a specific relationship between current and temperature. Besides, both of them are related to electric field as below equation according to Fowler-Nordheim tunneling theory.

$$J \propto E^2 exp\left(-\frac{K}{E}\right), K = 8\pi\frac{\sqrt{2m^*\phi_B^3}}{3qh}$$

E is intensity of electric field, m* is effective mass of carrier, ϕ_B is height of junction barrier energy, q is electron charge and h is Planck constant.

2.3 Operation of Space Charge Limited Transistor (SCLT)

Space charge limited transistor (SCLT) is developed from field effect transistor and this concept is shown in Fig. 2-6. Because of the low carrier mobility of organic semiconductor, enhancement of output current requires shortening the carrier channel length or raising the operating voltage. However, the former requires expensive photolithograph techniques and instruments, and the latter may lead to breakdown of devices. Both of them cannot fulfill our requirement of operating at low voltage.

The channel length of a vertical SCLT depends on the thickness of semiconductor. The thickness of semiconductor can be controlled by changing the solution concentration or the speed of spin coater, indicating the channel length can be easily controlled. SCLT is a vertical transistor composed of three terminals including emitter, base and collector. Carriers are

injected from emitter and are accepted in collector, while base is used to switch the current. This device used ITO glass as substrate, organic materials are formed by spin-coating, and electrodes are deposited by high vacuum thermal evaporator. Besides, the processes of porous structures will be demonstrated in chapter 3.

SCLT, defined by the carrier injection direction, can be separated into bottom-injection SCLT and top-injection SCLT. For bottom-injection SCLT, emitter is ITO and Al is collector; for top-injection SCLT, emitter is MoO3/Al and collector is ITO as shown in Fig. 2-7.

Operation of SCLT is similar to vacuum tube theory. Additional bias at base forms energy barriers in porous channel, and current can be controlled. In off state, there is a high energy barrier in porous base, and carriers from emitter can hardly go through this barrier resulting in little output current. In on state, the energy barrier in porous base is reduced or even disappears, and carriers can reach collector leading to large output current. The relationship between operation of SCLT and band diagrams is showed in Fig. 2-8.

2.4 Carrier Transport Mechanism of Metal-Oxide Semiconductors

In this section, the transport mechanism of amorphous indium gallium zinc oxide (a-IGZO) is briefly demonstrated. The carrier transport mechanism and electronic structure in an amorphous oxide semiconductor is similar to that of crystalline IGZO (sc-IGZO), and is explained by percolation conduction through potential barriers in the vicinity of conduction band edge. The potential barriers are thought to originate from random distribution of Ga^{3+} and

Zn^{2+} ions in the $GaO^{+}(ZnO)_5$ layer. The effective mass of a-IGZO was 0.34 m_e, which is almost the same as that of crystalline IGZO. These results imply the electronic structure and carrier transport mechanism in a- IGZO are similar to that in sc-IGZO, which would be associated with the electronic structure of metal-oxide semiconductors in which electron transport paths are made of spherical extended s orbitals and are not largely affected by local distortion of the chemical bonds [33]. The intermediate region shown in Fig. 2-9 (10^{14} $cm^{-3}<N_e<N_{th}$), the carriers still need to flow over the potential barriers as E_F is below E_{th}, leading to the thermally activated percolation behaviors in μ and σ. When E_F exceeds E_{th} at $N_e>N_{th}$, the carriers are not affected by potential barriers anymore and exhibit the temperature-independent extended mobility [34].

Each sub-element in the ternary material of a-IGZO film affects the parameters of TFT. It is expected the increase of In concentration increases carrier concentration [25]. Because indium atom is large, it is easy to lose electrons. The released electrons from In may be caught by oxygen or move to the conduction band when a-IGZO film lacks of oxygen [35]. Therefore the carrier transportation can be enhanced. In addition, gallium in a-IGZO film provides high stability for a-IGZO TFT [36]. Gallium in a-IGZO film can reduce electron concentration and mobility. Ga was chosen because atomic radius of Ga is close to In. Hosono *et al.* reported that Ga^{3+} in a-IGZO film tightly attracts oxygen due to high ionic potential resulted from small ionic radius and +3 valance. As a result, injection of electrons is

suppressed and oxygen ions escaping from a-IGZO film are induced [37]. Compared with indium zinc oxide (IZO), the carrier concentration of a-IGZO (~10^{19} cm^{-3}) is smaller than that of IZO (~10^{21} cm^{-3}) [37-39]. Besides, Ga also reduces the sensitivity of carrier concentration to the variation of O_2/Ar ratio [39], indicating Ga helps a-IGZO film to control carrier concentration. However, the reduced mobility accompanies with the addition of Ga also. Hosono *et al.* reported that oxygen molecules are doped to increase carrier concentration and mobility in the presence of Ga in a-IGZO film [40]. Zinc in a-IGZO film was reported to affect the crystallization of the thin film. Crystalline structure was reported with the ratio of Zn in a-IGZO film lager than 65% [35]. The crystalline structure in a-IGZO film may cause degradation of electrical characteristics while the uniformity was reduced by the disordered grain boundaries.

2.5 Methods of Device Parameters Extraction

In this section, the extractions of the device parameters are discussed in details. The field effect mobility, turn on voltage (V_{on}), the on/off current ratio (I_{on}/I_{off}), and the sub-threshold swing (S.S) are extracted and assessed, respectively.

2.5.1 Mobility (μ)

Mobility is a measurement of the velocity of the carrier moving through a material. High mobility allows high frequency response which is the time taken for the device to transfer from off state to on state. In the off state, little current flows through the device. In the on state, large

amount of currents flows through the device. A large mobility indicates large output current. The mobility in this study refers to the saturation mobility which is extracted from the saturation region. The device is operated at drain voltage (V_{DS}) of 20 V, since the threshold voltage (V_{TH}) is much lower than 20V. The saturation mobility is determined from the transconductance (g_m) defined as Eq. 2-1.

$$g_m = \left[\frac{\partial\sqrt{I_{DS}}}{\partial V_{GS}}\right]_{V_{DS}=\text{const}} \quad \text{Eq. 2-1}$$

The drift component of drain current in saturation region is as Eq. 2-2.

$$I_{DS} = \frac{1}{2}\mu C\frac{W}{L}(V_{GS} - V_{TH})^2 \quad \text{Eq. 2-2}$$

When the mobility is determined, I_{DS} in Eq. 2-1 is replaced by Eq. 2-2.

$$g_m = \sqrt{\frac{W\mu C}{2L}}$$

The saturation mobility (μ_{sat}) is solved as followed.

$$\mu_{sat} = \left[\frac{2g_m^2}{\frac{W}{L}C}\right]_{saturation}$$

C is the capacitance of gate insulator, W is channel width, and L is channel length.

2.5.2 Turn-On Voltage (V*on*)

Turn-on voltage (V_{on}) is defined as the gate voltage at which the drain current begins to increase in a transfer curve. V_{on} can directly characterize the gate voltage required to fully turn off the transistor in a switching application.

2.5.3 Threshold Voltage (V_{TH})

Threshold voltage is related to the operation voltage and power consumptions of TFTs. We

extract the threshold voltage from Eq. 2-3, the intercept point of the square-root of drain current versus voltage when devices operate in saturation mode

$$\sqrt{I_{DS}} = \sqrt{\frac{W}{2L}\mu C}(V_{GS} - V_{TH}) \quad \text{Eq. 2-3}$$

2.5.4 I_{on}/I_{off} Current Ratio

The I_{on}/I_{off} (on/off) ratio represents the ratio between large turn-on current and small off current. It is an indicator of how well a device will work as a switch. A large on/off current ratio means there are enough turn-on current to drive the pixel and low off current to maintain in low consumption.

2.5.5 Sub-Threshold Swing (S.S.)

Another important characteristic for device application is sub-threshold swing (S.S.). It is a measurement of how rapidly the device switches from off state to on state. Moreover, the sub-threshold swing also represents the interface quality and the defect density. Sub-threshold swing is defined as followed. If we want to have a better performance TFTs, we need to lower the sub-threshold swing.

$$S.S. = \left[\frac{\partial V_{GS}}{\partial(\log I_{DS})}\right]_{V_{DS}=\text{const}}$$

Figures of Chapter 2

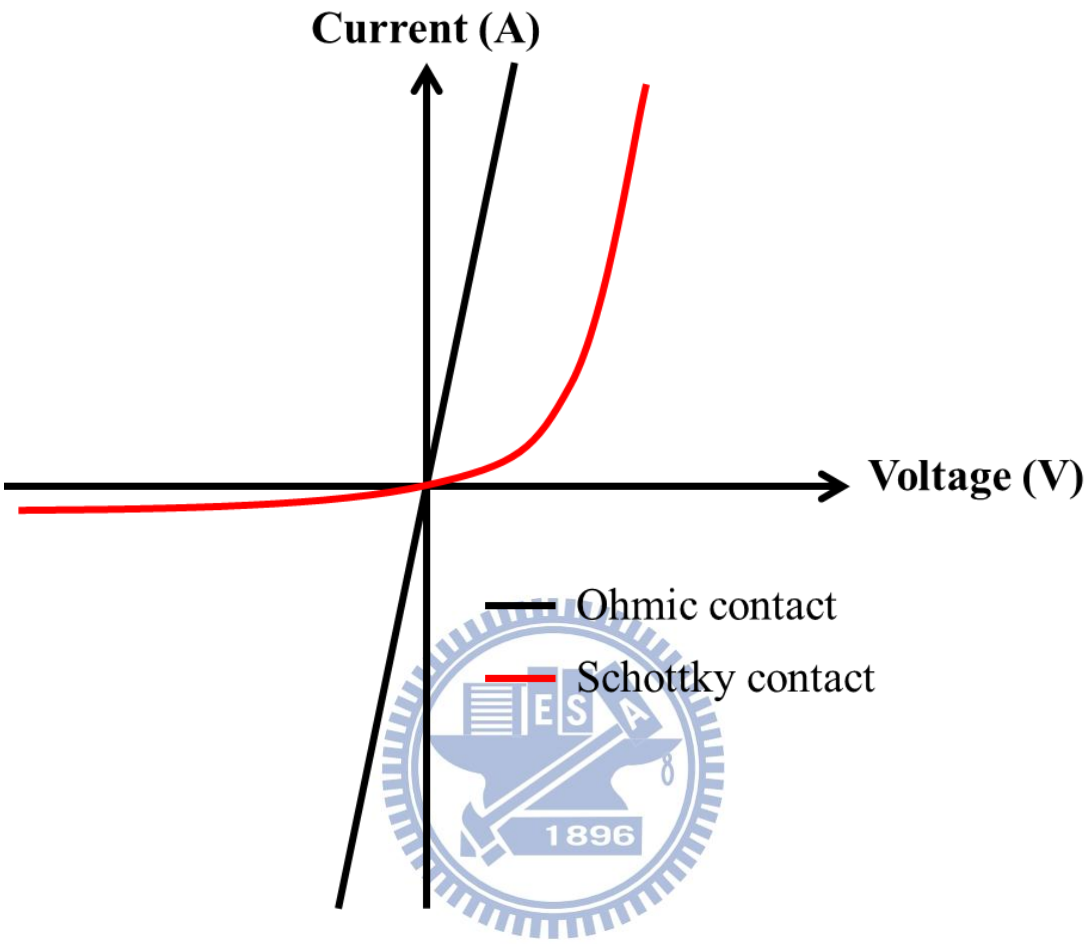

Fig. 2-1 The characteristics of current as a function of voltage. Both ohmic contact and schottky contact are shown.

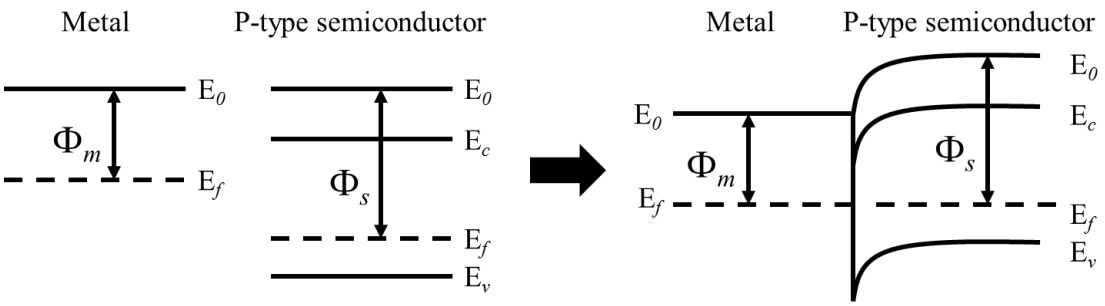

Fig. 2-2 Band diagram of schottky contact.

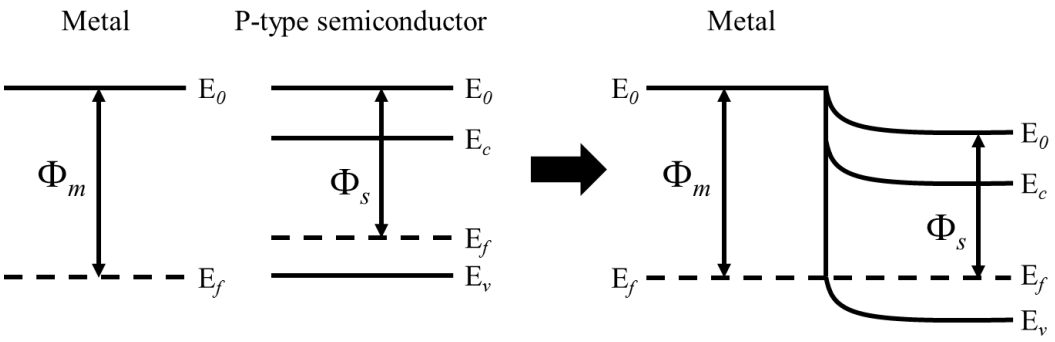

Fig. 2-3 Band diagram of ohmic contact.

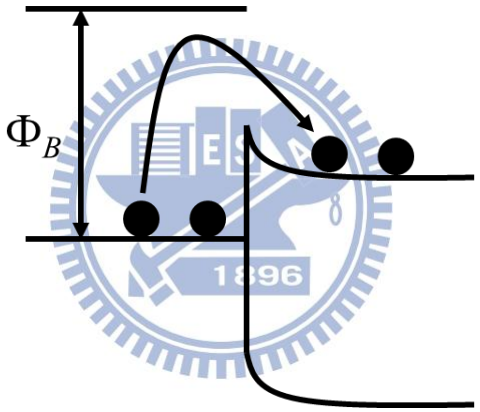

Fig. 2-4 Schematic diagram of thermionic emission theory.

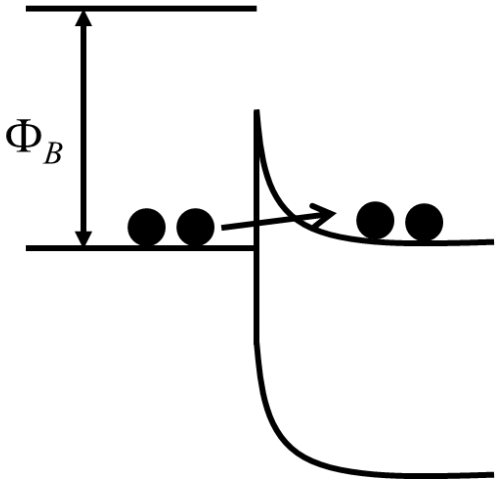

Fig. 2-5 Schematic diagram of tunneling effect.

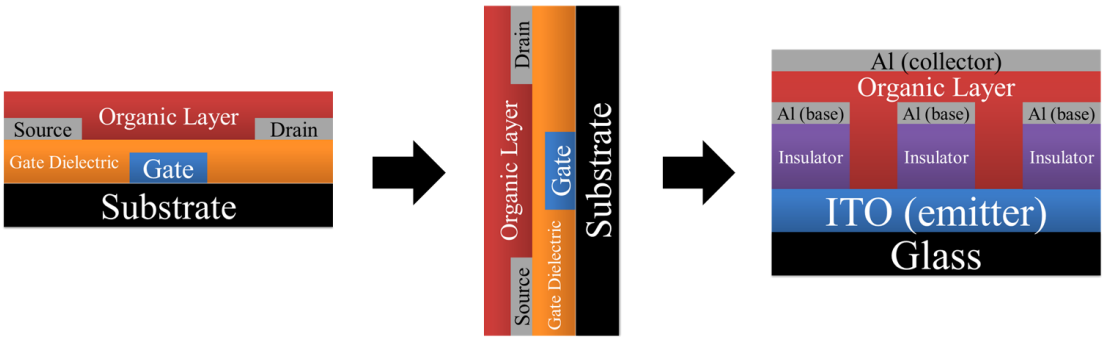

Fig. 2-6 Development of space charge limited transistor (SCLT) from field effect transistor.

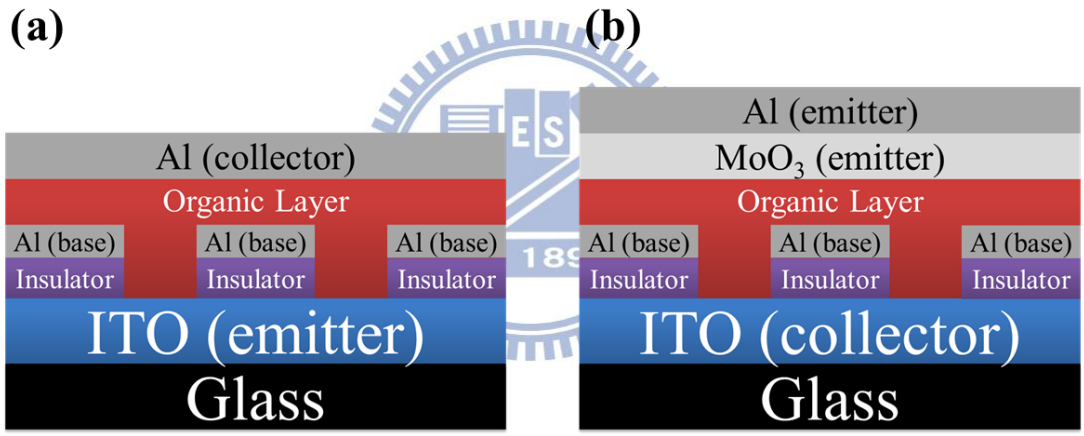

Fig. 2-7 Structures of bottom-injection and top-injection SCLTs. (a) Bottom-injection SCLT, emitter is ITO and Al is collector. (b) Top-injection SCLT, emitter is MoO_3/Al and collector is ITO.

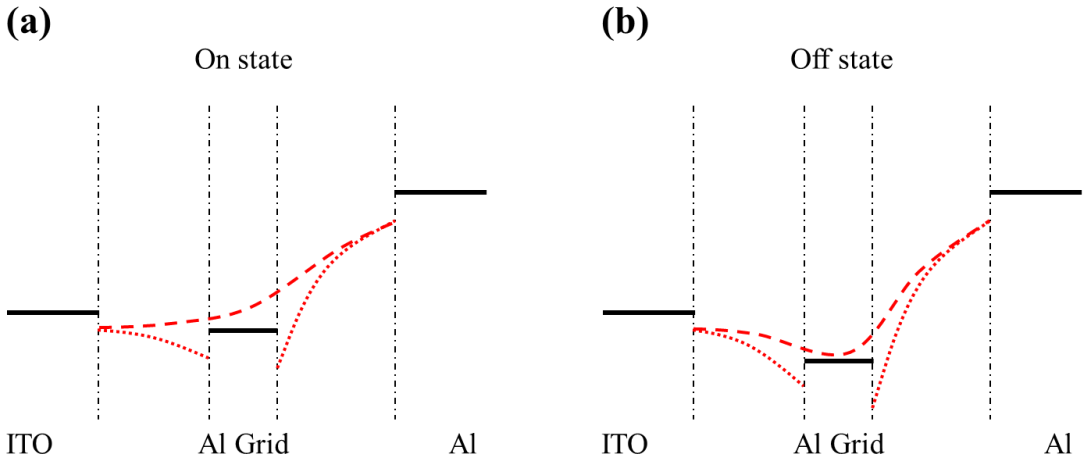

Fig. 2-8 The relationship between operation of SCLT and band diagrams. (a) On state of SCLT. (b) Off state of SCLT.

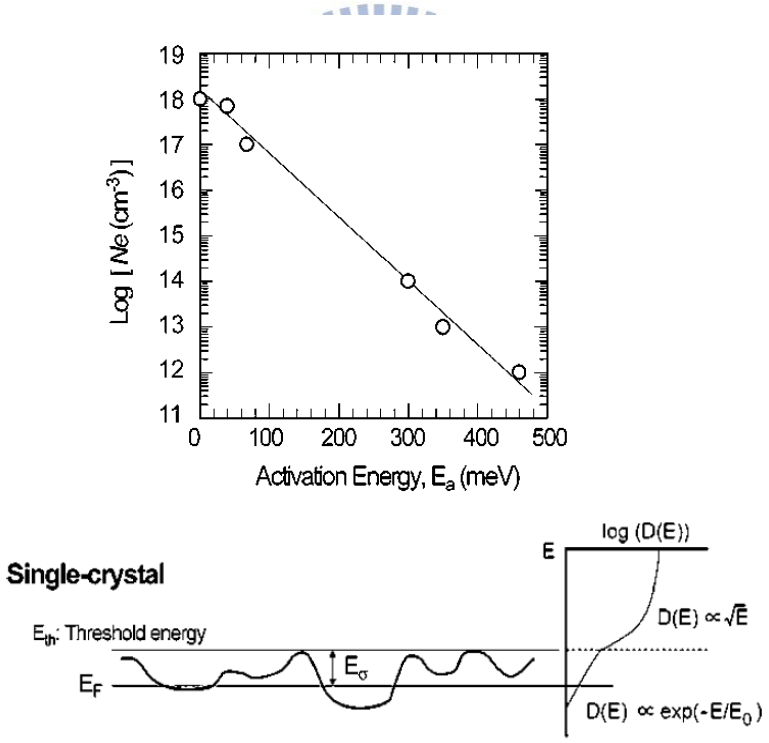

Fig. 2-9 (a) The relationship between log(N_e) and activation energy (E_a). The straight line is the result fitted to the exponential tail density of state model. (b) Schematic energy diagram near the conduction band edge and the density of state for sc-IGZO [34].

Chapter 3 Device Fabrication and Experiment Setup

3.1 Introduction

In this chapter, the fabrication processes, structures of devices and material analysis tools used will be briefly introduced. During the processes, glove boxes filled with nitrogen were used to prevent our devices from oxygen and vapor.

3.2 Space Charge Limited Transistor (SCLT) Sensor

In the section, the processes of vertical P3HT-based space charge limited transistor (SCLT) sensors based on ITO glass substrate are demonstrated. The electrodes of SCLT are emitter (E), base (B), and collector (C). Indium tin oxide (ITO) is used as emitter electrode, while aluminum (Al) is used as base and collector electrodes. Active region of SCLT sensor is 1x1 cm^2. Three-dimensional and two-dimensional SCLT sensor schematic diagrams are shown in Fig. 3-1; a scanning electron microscope (SEM) image of SCLT is shown in Fig. 3-2. All the fabrication steps were processed in glove box, except for glass substrate cleaning, ITO patterning, and adherence of polystyrene (PS) balls. The flowchart of the fabrication processes is showed in Fig. 3-3.

3.2.1 Glass Substrate Cleaning

Resistance and thickness of ITO on glass substrate were <7Ω and 200 nm. Before cleaning, we divided the ITO glass substrate into 3x3cm^2 squares. The purpose of substrate

cleaning was to remove particle and organic pollution on glass substrate. The followings were procedures of glass substrate cleaning. First, Immerse the glass substrate in the streaming DI water for 5 minutes: to remove particles. Second, put glass substrates into acetone (ACE) under ultrasonic resonance for 10 minutes: to remove organic pollution. Third, immerse the glass substrate in the streaming DI water for 5 minutes: to remove the residue of ACE. Fourth, put glass substrates into isopropanol (IPA) under ultrasonic resonance for 10 minutes: to remove organic pollution. Fifth, immerse the glass substrate in the streaming DI water for 5 minutes: to remove the residue of IPA. Sixth, use N_2 to quickly blow off water drops remained on the substrate to prevent spots of water. Finally, put glass substrates on the hot plate at 120℃ for 5 minutes to remove the residual moisture and then cool down to the room temperature.

3.2.2 ITO Patterning

To define the ITO electrodes, the shadow mask was used. The processes of ITO patterning are as follow. First, put the cleaned ITO glass substrates on the hotplate at 170℃ for 10 minutes. Then rapidly stick the negative photoresist (PR) onto the glass substrates once ITO substrates leave the hot plate. Second, use the defined shadow mask and exposure to UV lithography to define ITO patterns. Third, immerse the patterned substrates into K_2CO_3 solution of which the formula ratio is 50mg K_2CO_3 to 1000ml water for 50 to 80 seconds to develop. After that, use DI water to clean, and then remove the residue PR by tissues. Fourth, use 36wt% Hydrogen chloride (HCl) solution at 50℃ to 60℃ for 50 seconds to etch the

un-developed ITO, and then use DI water to clean. Finally, use 5 wt% sodium hydroxide (NaOH) solution to remove PR and then use DI water to clean.

3.2.3 ITO Surface Planarization

Before forming insulator layer, Oxygen plasma at power of 100 W was used to treat the ITO surface for 10 min. The purpose was to planarize the roughness of ITO surface.

3.2.4 Insulator Layer

Cross-linkable poly(4-vinyl phenol) (PVP) (8 wt.%) (Mw approx. 20000, Aldrich) and cross-linking agent poly(melamine-co-formaldehyde) (PMF) were dissolved in propylene glycol monomethyl ether acetate (PGMEA) with a PVP:PMF mass ratio of 11 : 4.

With 8wt% PVP solution, insulator layer was formed with PVP solution by spin-coating on the patterned ITO glass substrate in the glove box. Then annealing at 200℃ for 1 hour was used to make PVP form cross-link. The thickness of PVP after annealing was 200 nm measured by Kosaka Laboratory Ltd., ET-4000.

3.2.5 Sacrificing Layer

A 1.5 wt% poly(3-hexylthiophene-2,5-diyl) (P3HT) (RR ＞ 98.5%, Rieke Metals Inc.) solution dissolved in chlorobenzene (CB) was used to form the sacrificing layer by spin-coating at 5000 rpm for 30 seconds on the PVP layer in the glove box. After that, 200℃ annealing for 10 minutes was used. Thickness of the layer was about 20 nm.

3.2.6 Spin-Rinse

p-Xylene (4 drops) was used to spin-rinse the sacrificing layer by spin-coating at 7000 rpm for 60 seconds. After this process, it decreased the thickness of sacrificing layer by 10 nm and increased the P3HT surface polarity.

3.2.7 Adherence of Polystyrene Balls

In this step, 0.4 wt% negatively charged polystyrene (PS) balls (Fluka-90517, diameter = 100 nm; Fluka-95581, diameter = 200 nm) solution dissolved in ethanol was used. After spin-rinse, immerse the substrate into the 0.4 wt% PS balls solution for 90 seconds at first. Then take the substrate out off the PS balls solution and use ethanol to clean. Finally, immerse the cleaned substrate into boiling 220℃ IPA for 10 seconds, and then use nitrogen to blow the substrate dry immediately.

3.2.8 Porous Base Electrode

With PS balls adhering to the sacrificing layer, 40 nm-thick Al served as the base electrode (B) was deposited onto the substrate by thermal evaporation at the rate of 0.2 nm/s. Then scotch tape (3M) was used to remove the PS balls covered with Al, and the left Al comprised porous base electrode with revealed PVP insulator layer.

3.2.9 Vertical Channel

With porous base electrode as hard mask, oxygen plasma at 100 W for 10 minutes was used to etch the exposed PVP down to ITO electrode. After oxygen plasma treatment,

cylindrically vertical channels were formed.

3.2.10 Active Layer

A 350 nm active layer was composed of 4.5 wt% P3HT solution dissolved in CB by spin-coating at 1500 rpm for 40 seconds. After spin coating, the substrate with P3HT-based active layer was annealed at 200℃ for 10 minutes.

3.2.11 Porous Collector Electrode

After annealing the active layer, the substrates were treated with spin-rinse mentioned in step (6) and adherence of PS balls mentioned in step (7) in order. With PS balls adhering to the active layer, 40 nm-thick Al served as collector electrode (C) was deposited onto the substrate by thermal evaporation at the rate of 0.2 nm/s. Finally, Scotch tape (3M) was used to remove the PS balls covered with Al, and the left Al comprised porous collector electrode with revealed P3HT-based active layer.

3.3 Amorphous IGZO TFT Hybrid Sensor

In this section, the fabrication of a-IGZO TFTs hybrid sensor including processes of a-IGZO TFTs and capping of $W_{18}O_{49}$ as sensing layer are demonstrated. Two-dimensional a-IGZO TFT hybrid sensor schematic diagram is shown in Fig. 3-4. The a-IGZO TFT here is bottom gate top contact with heavily p-doped Si wafer as gate electrode, 100 nm silicon nitride (SiNx) as gate dielectric, and 100nm Al as source and drain (S/D) electrodes. Channel length and width of a-IGZO TFT are 200 μm and 1000 μm respectively. Besides, $W_{18}O_{49}$ is

from Prof. Chi-Chuang Hu of National Tsing Hua University. A scanning electron microscope (SEM) image of $W_{18}O_{49}$ is shown in Fig. 3-5.

3.3.1 Gate Dielectric Layer

A gate dielectric layer was deposited on a 6-inch heavily p-doped silicon wafer by low pressure chemical vapor deposition (LPCVD) of National Nano Device Laboratories at 780℃ with gases of NH_3 and SiH_2Cl_2. After deposition of SiNx, there was SiNx on both sides of the p-doped silicon wafer. Reactive ion etching (RIE) was used to remove the SiNx on the back side of the wafer and the revealed silicon was used as gate electrode. Process gases during RIE were oxygen (O_2) 5 sccm and tetrafluoromethane (CF4) 80 sccm. Besides, process pressure and RF power were 15.0 Pa and 100W.

3.3.2 Substrate Cleaning

The 6-inch heavily p-doped Si wafer with SiNx on one side was split into 3×3 cm^2 squares at first. Before deposition of active layer – IGZO film, the spilt substrates should go through the standard clean composed of SC1 and SC2. The capability of SC1 and SC2 were to remove microscopic particles and alkali metal ions on the surface of substrates respectively. The first step of standard clean was using N_2 to blow off macroscopic particles and flushing the substrates with DI water for 5 minutes. Second, immerse substrates into SC1 solution for 10 minutes. SC1 solution was composed of ammonium hydroxide (NH_4OH), hydrogen peroxide (H_2O_2) as oxidant, and 75 ~ 85 ℃ DI water with the formula: NH_4OH: H_2O_2: H_2O =

1: 4: 20. Third, flush the substrates with DI water for 5 minutes. Fourth, immerse the substrates into SC2 solution for 10 minutes. SC2 solution was composed of HCl, H_2O_2 as oxidant, and 75 ~ 85 ℃ DI water with the formula: HCl: H_2O_2: H_2O = 1: 1: 6. Finally, flush the substrates with DI water for 5 minutes and use N_2 to quickly blow off water drops remained on substrates to prevent spots of water.

3.3.3 a-IGZO Film Deposition

Radio-frequency (rf) sputter and a 3-inch circular IGZO target (In: Ga: Zn: O = 1: 1: 1: 4 at%) were used to deposit 30 nm a-IGZO film at room temperature with rf power of 100W, working pressure of 0.009 torr, and O_2/(Ar+ O_2) ratio of 0.098%. The pattern of a-IGZO was defined by shadow masks.

3.3.4 Post-Annealing

After rf sputtering a-IGZO, 400℃ the substrates with a-IGZO film were post-annealed at atmospheric pressure for 1 hour in a nitrogen furnace. The flow rate of nitrogen was 10 liter per minute (L/m).

3.3.5 Source/Drain Deposition

100 nm Al was deposited as source/drain electrodes by thermal evaporator. Patterns of source/drain were defined by shadow masks. The deposition was started at the pressure < 5×10^{-6} torr and depositing rate was controlled at 0.2 nm/s.

3.3.6 Sensing Layer Capping

Through step 1 to 5, the a-IGZO TFT was fabricated. Basing on a-IGZO TFT, $W_{18}O_{49}$ was capped as sensing layer. There were two methods to cap $W_{18}O_{49}$ which are drop and spin-coating. They would be introduced respectively as follow.

Drop-coating

Before drop coating $W_{18}O_{49}$, a-IGZO TFTs were heated to 85℃. Then $W_{18}O_{49}$ solution dissolved in ethanol was dropped onto the channel of a-IGZO TFTs. Finally, wait for the evaporation of ethanol.

Spin-coating

Before spin-coating $W_{18}O_{49}$, a-IGZO TFTs, a-IGZO TFTs were irradiated by ultraviolet (UV) rays for 5 minutes. After irradiation of UV rays, $W_{18}O_{49}$ were spun onto the channel of a-IGZO TFTs at 500 rpm for 30 seconds. Then put the a-IGZO TFTs on 85℃ hotplate for 5 minutes to evaporate ethanol, and one layer of $W_{18}O_{49}$ was formed. By repeating the above processes, more than one layer of $W_{18}O_{49}$ could be formed.

3.4 Micro-fluid Gas Sensing Measurement System

Gas sensing of SCLT sensor and a-IGZO TFT hybrid sensor is operated in the micro-fluid gas sensing measurement system shown in Fig. 3-6. A sensor was placed in a micro-fluid sensing chamber containing an atmosphere of high purity (99.9999%) nitrogen (N_2) gas. For ammonia (NH_3) gas sensing, an electrical syringe pump system was used to inject the NH_3 (99.9999% pure) gas into a tube to mix with the N_2. The gas mixture then entered the

micro-fluid system; for nitric oxide (NO) sensing, the NO (10,000 ppm diluted in N_2) gas was directly injected into a tube to mix with the N_2. The amounts of N_2 and NO were controlled by mass-flow controllers. Specific concentrations of NH_3 and NO were obtained by adjusting the injection speed of the syringe pump and by adjusting the flow rate of NO by the mass-flow controller respectively. The sensing results were measured by Keithley 2400 connected to a computer.

3.5 Analysis Instruments

3.5.1 Current-Voltage Measurement Instruments

The instruments used for current and voltage measurement were Agilent E5270B and Keithley 2400. Agilent E5270B was used to measure the electrical characteristics, while Keithley 2400 was used during gas sensing.

3.5.2 Radio Frequency Magnetron Sputter

A radio frequency of 13.56 MHz is used to generate plasma. The generated plasma creates ions to sputter the target material. Ions are accelerated towards the target by a negative DC bias on the target. Generally, the RF sputtering is operated at the pressure of 0.05 torr to improve the quality and the deposition rate of the deposited film. The quality of the film deposited at the low pressure is increased due to the increase of mean free path contributing to the species to find a stable state.

Figures of Chapter 3

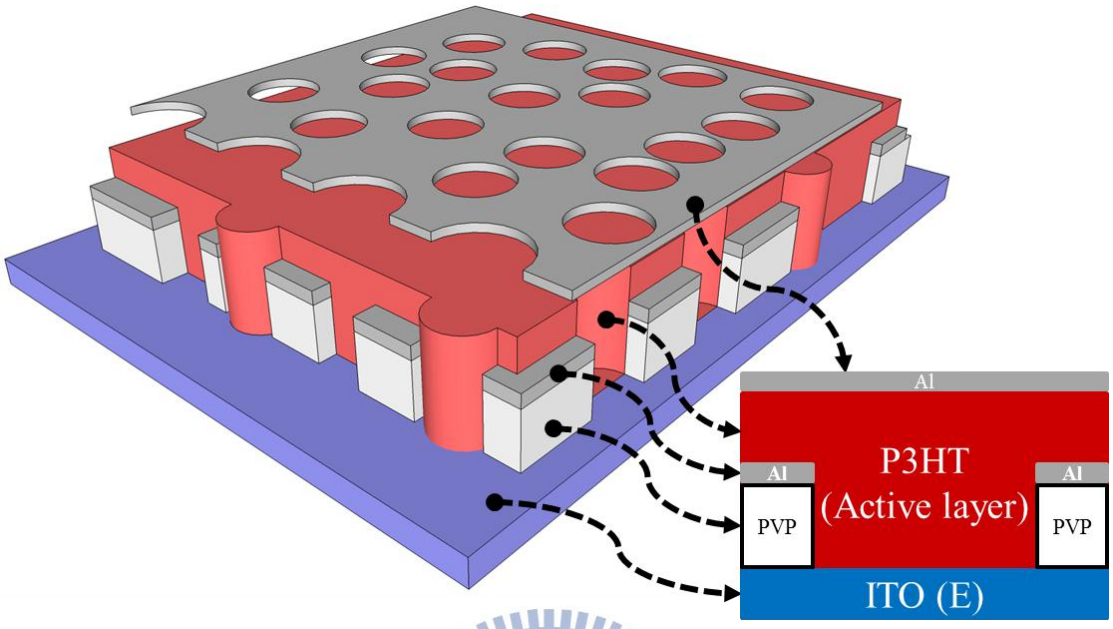

Fig. 3-1 The three-dimensional and two-dimensional SCLT schematic diagrams.

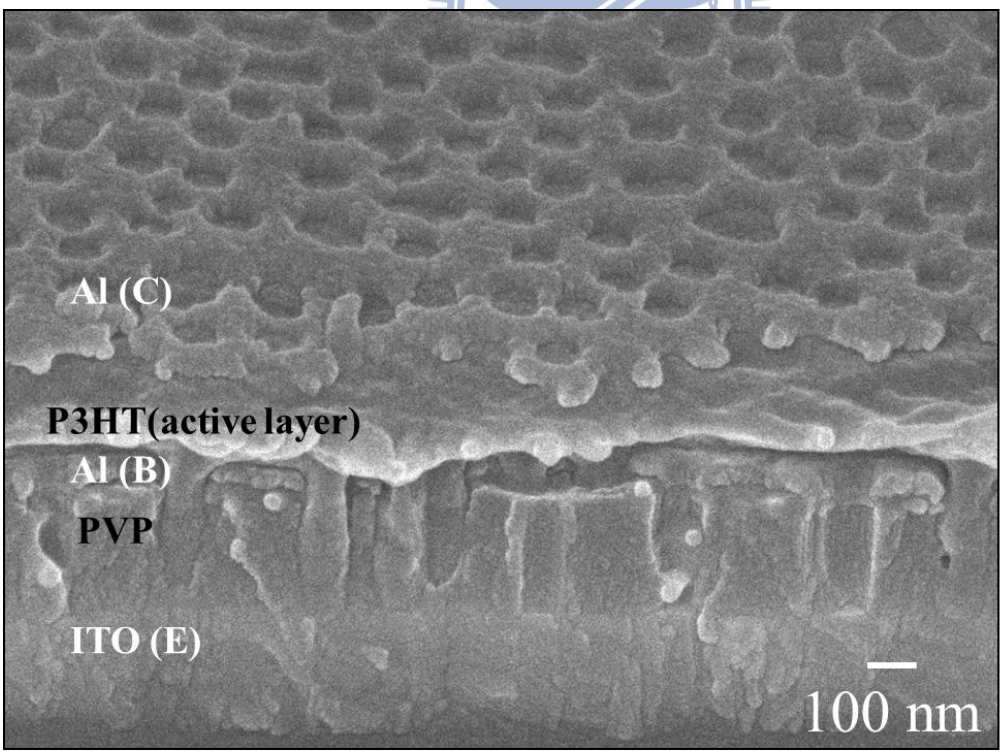

Fig. 3-2 The SEM cross-section image of SCLT.

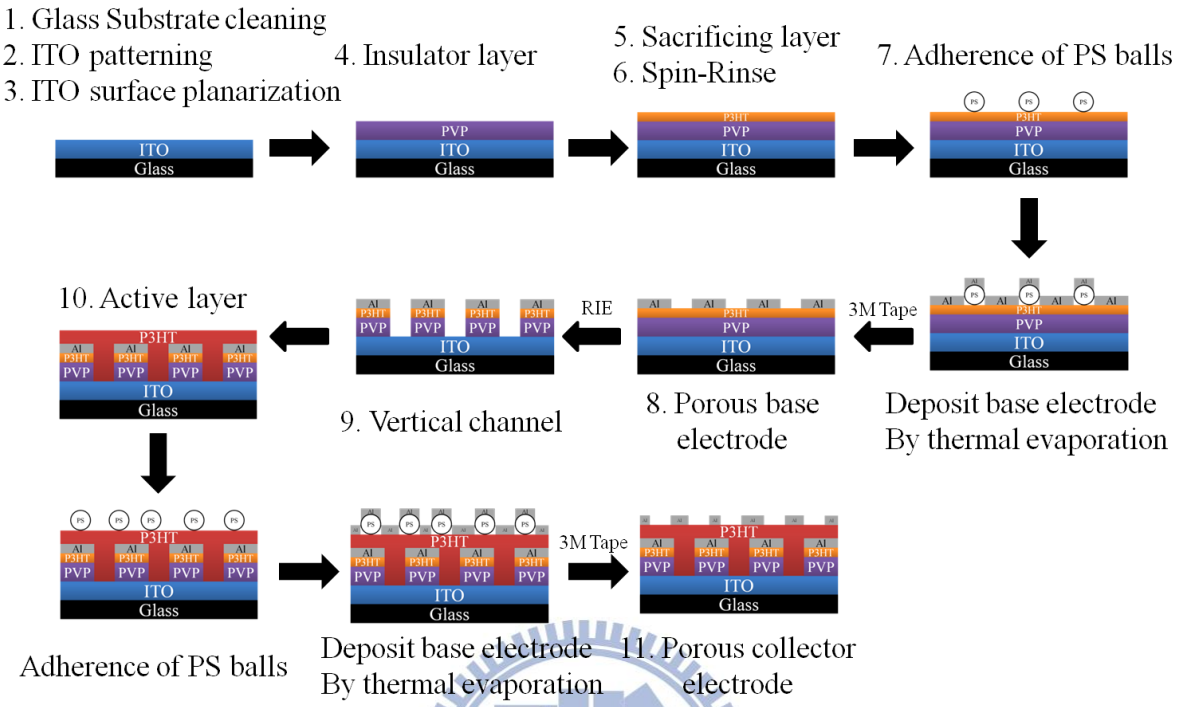

Fig. 3-3 The flowchart of the fabrication processes of SCLT sensor.

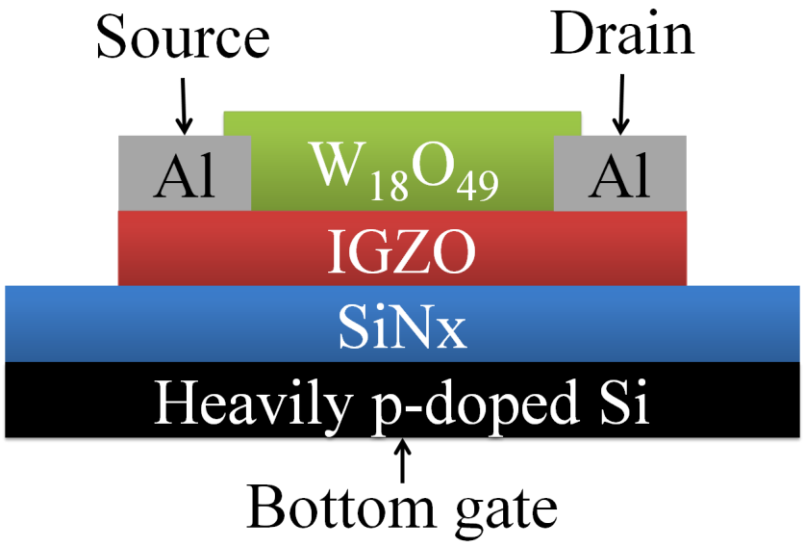

Fig. 3-4 Two-dimensional a-IGZO TFT hybrid sensor schematic diagram.

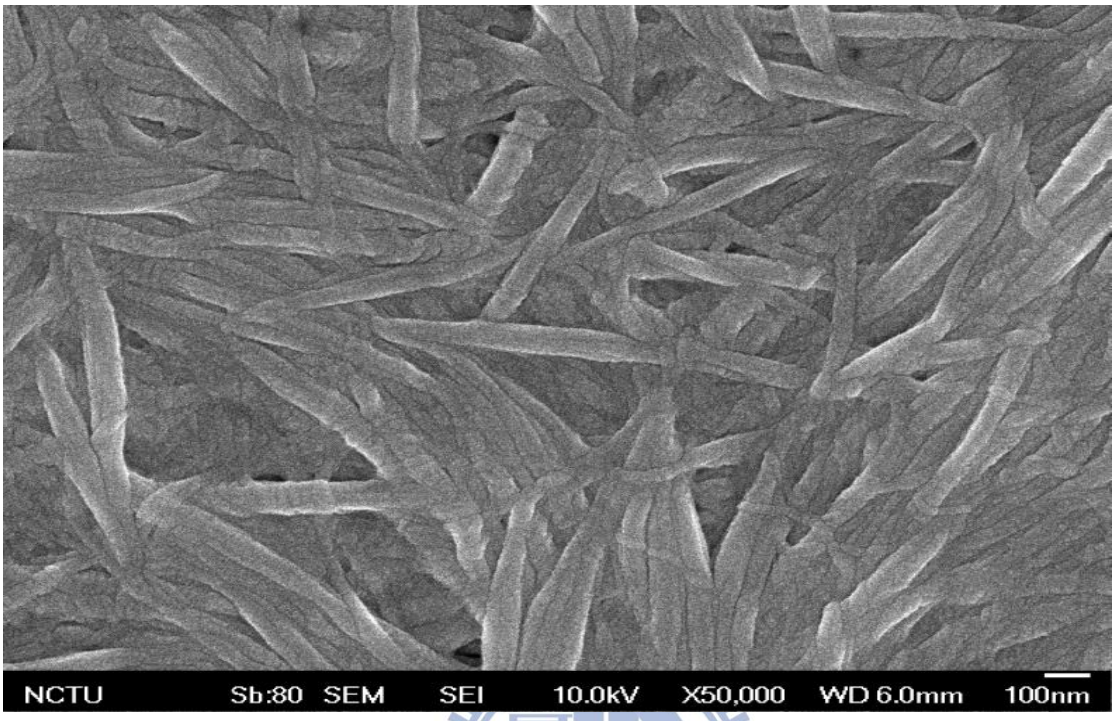

Fig. 3-5 A scanning electron microscope (SEM) image of $W_{18}O_{49}$.

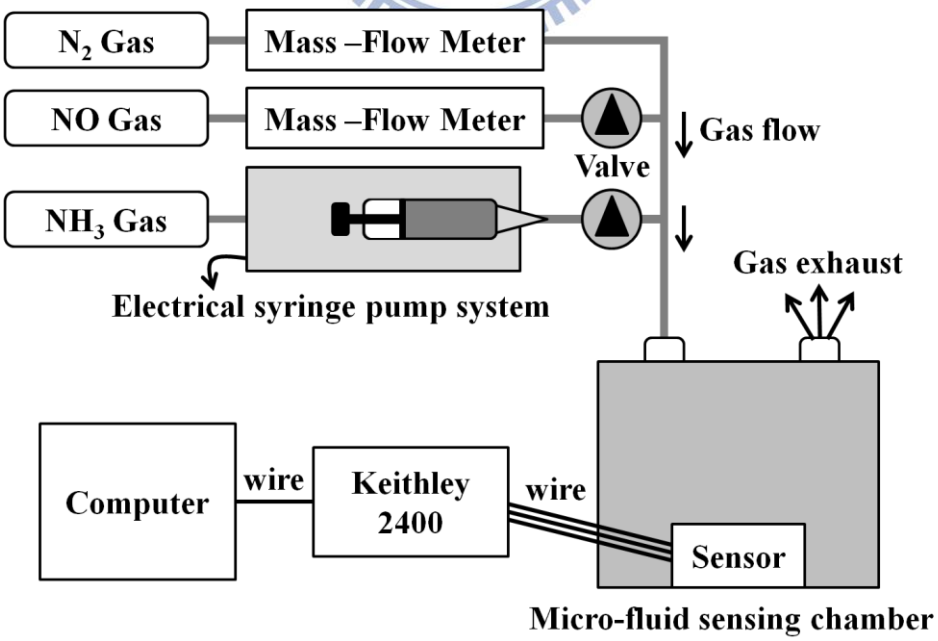

Fig. 3-6 Micro-fluid gas sensing measurement system.

Chapter 4 Results and Discussion

4.1 Space Charge Limited Transistor (SCLT) Sensor

In this section, we demonstrate that the low switching swing of SCLT is critical to provide high gas sensitivity. The lowest detectable ammonia concentration is 30 ppb for a poly(3-hexylthiophene) (P3HT) SCLT. On the other hand, for P3HT OTFT with a conventional bottom-gate structure, the detection limit to ammonia gas is larger than 1 ppm [41]. The high sensitivity to ammonia achieved in this section enables the development of non-invasive breath ammonia analysis for monitoring dysfunction of the human body [42]. For such applications, a portable and real-time ammonia sensor with a detection limit of 50 ppb is critical, but is still challenging [42]. Besides, 30 ppm nitric oxide gas sensing were also demonstrated. Our results may facilitate the development of low-cost point-of-care technology.

4.1.1 Characteristics of Porous SCLT

Before analyzing the experimental gas sensing response, the diode characteristics of the SCLT with porous collector (porous SCLT), including EC, EB and BC diode, are shown in Fig. 4-1 to confirm well injection of holes from emitter to collector and no leakage current between EB and BC. During diode measurement, additional bias is added to the former electrode while the latter one is grounded. EC diode as example, additional bias is added to emitter and collector is grounded. Besides, the output characteristics, the collector current density (J_{CE}) as a function of the collector voltage (V_{CE}), of the porous SCLT are shown in

Fig.4-2. With collector bias (V_{CE}) as -2.4 V and -1.2 V, porous SCLT exhibits an on/off current ratio as 4750 and 890, and a switching swing as 140 mV/dec. and 122 mV/dec., respectively. Fig. 4-3 shows the transfer characteristics, the collector current density (J_{CE}) as a function of the base voltage (V_{BE}), of porous SCLT. Two test gas sensing responses, the NH_3 as the e-doping gas and the NO as the e-dedoping gas, are investigated [43]. Gas sensing were operated through micro-fluid gas sensing measurement system shown in Fig. 3.5-1.

4.1.2 Ammonia Sensing Results

In this section, results of NH_3 sensing are demonstrated. The response sensitivity to NH_3 is defined as follows:

$$\text{Sensitivity} = \frac{\Delta J}{J_0} = \frac{J_{CE}-J_{CE0}}{J_{CE0}} \quad \text{Eq.4.1-1}$$

where J_{CE} and J_{CE0} are the collector current density exposed to NH_3 for 200 second and the one before NH_3 exposure respectively from transfer characteristics (J_{CE}-V_{BE} curve).

Effect of Collector Voltage (V_{CE}) on Sensitivity

The relationship between sensitivity and V_{CE} is demonstrated at first. Fig. 4-4 shows a plot of sensitivity to NH_3 concentration with three different V_{CE} bias conditions. The NH_3 concentrations were ranged from 30 ppb to 1000 ppb; the V_{CE} bias conditions are -1.2 V, -1.8 V and -2.4 V. With collector bias (V_{CE}) as -1.2 V, porous SCLT exhibits the maximum sensitivity to NH_3.

Carrier Injection Effect on Sensitivity

In this section, two structure of porous SCLT shown in were utilized to study the effect of carrier injection. Because injection of holes is from emitter to collector, we can change the injecting direction of holes, i.e. bottom-top or top-bottom, by using different metal as emitter and collector. For bottom injection of holes, ITO and Al were used as emitter and collector respectively. For top injection of holes, MoO_3/Al and ITO were used as emitter and collector respectively. Fig 4-5 shows a plot of sensitivity as a function of NH_3 concentration with different injection of holes and the NH_3 concentrations were ranged from 10 ppb to 1000 ppb. We can find that the response of bottom injection is higher than top injection. The mechanism is still unknown to explain the better sensitivity of bottom injection structure. However, as shown in Fig. 4-6, it is supposed that hole concentration in the bulk area (the exposing area) of P3HT is higher for top injection than that for bottom injection, indicating the proportion of holes reacted with NH_3 is relatively smaller than bottom injection which has less hole concentration in bulk region. As a result, the response of bottom injection is higher.

Effect of Base Voltage (V_{BE}) on Sensitivity

Fig. 4-7(a) shows a plot of J_{CE}-V_{BE}, representing the porous SCLT's sensing response to NH_3. V_{CE} was fixed as -1.2 V and the NH_3 concentrations were ranged from 30 ppb to 1000 ppb. The response of the switching region (V_{BE} = -0.4 V to 0 V) of J_{CE}-V_{BE} plot is shown in Fig. 4-7(b). Increasing NH_3 concentration makes J_{CE}-V_{BE} curves shift to the left. Because

NH_3 acts as electron doping (e-doping) agents, increasing NH_3 concentration indicates increasing e-doping concentration in P3HT which turns out to be the increase of the potential barrier. Therefore, a more negative base potential is required to lower down the channel potential barrier and to turn on the transistor. The sensing sensitivities $\triangle J/J_0$ as a function of V_{BE} for various NH_3 concentrations are plotted in Fig. 4-8(a). We found that the sensitivity was strongly dependent on V_{BE}, and that the maximum sensitivity occurred in the switching zone ($-0.5\ V < V_{BE} < 0\ V$). For NH_3 concentrations of 30 ppb, 100 ppb, and 1000 ppb, the maximum sensitivities measured at V_{BE} = -0.2 V and V_{CE} = -1.2 V are -0.09, -0.23, and -0.56, respectively. As shown in Fig. 4-8(b), a power law relationship is found between the maximum sensitivity and NH_3 concentration, indicating that the proposed NH_3 sensor is particularly sensitive in low-concentration regime (i.e. 30 ppb to 1000 ppb). Besides, we also compare sensitivity of a SCLT sensor with that of a diode sensor (previous results by M. Z. Dai) in Fig. 4-8(b). For diode sensor, ITO and porous Al were used as electrodes, and 300 nm P3HT acted as active layer and sensing layer. It shows that SCLT sensor exhibits a better sensitivity to NH_3. However, the mechanism to explain the difference between SCLT and diode sensors is still unclear.

SCLT Bias Stress on Sensing Response

As aforementioned, effect of NH_3 on porous SCLT makes J_{CE}-V_{BE} curves shift to the left and the maximum sensitivities were measured at V_{BE} = -0.2 V and V_{CE} = -1.2 V. However, the

effect of bias stress on SCLT makes J_{CE}-V_{BE} curves shift to the right. As shown in Fig. 4-9(a), J_{CE}-V_{BE} curves of porous SCLT, undergoing bias stress (V_{BE} = -0.2 V and V_{CE} = -1.2 V) for 4200 seconds, shifted to the right; after bias stress, porous SCLT was treated with NH_3 (100 ppb for 200 seconds) and J_{CE}-V_{BE} curves then shifted to the left. We found that the bias stress seems to affect sensing response. Fig. 4-9(b) shows the maximum sensitivity as function of the time after finishing of bias stress and NH_3 concentration is 100 ppb for 200 seconds. The sensitivity, right after bias stress, is higher than the others. It is supposed that J_{CE}-V_{BE} shifts to the right during bias stress, while J_{CE}-V_{BE} recovers back to the left after bias stress. In addition, the effect of NH_3 makes J_{CE}-V_{BE} shift to the left. Therefore, two effects, recovery and NH_3 together, make the shift of J_{CE}-V_{BE} much more dramatically indicating the increase of sensitivity. However, with the passage of time, the effect of recovery decreases. In the meanwhile, J_{CE}-V_{BE} shift is mainly dominant by the effect of NH_3 resulting in decrease of sensitivity.

Switching properties of the transistor under NH_3 sensing

Since the proposed sensor is embedded in a vertical transistor, it is therefore important to evaluate the switching properties of the transistor under NH_3 sensing. The switching function of the porous SCLT under NH_3 sensing is shown in Fig. 4-10. For NH_3 sensing, we want to emphasize the ability of switching between on and off states during NH_3 sensing or not. However, on/off ratio at Vce = -1.2V is not obvious to show the switching ability. Therefore,

we chose Vce = -1.7V at which have obvious on/off ratio as well as the good enough response to NH_3. The porous SCLT exhibits a significant current drop under NH_3 sensing (the shaded areas). During NH_3 sensing, a good on/off switching property is still obtained when switching V_{BE} between -0.9 V (on state) and 0.9 V (off state). This result suggests that the proposed porous SCLT integrates a NH_3 sensor and a switching transistor in one single device. In sensor array technology, to save the operational power and to improve the signal-to-noise ratio, the pixel circuit is composed of one sensor and one switching transistor [44]. Our proposed device can serve as a pixel circuitry by itself, facilitating the development of low-power sensor array technology.

Note that the poor recovering current after removing NH_3 gas attributed to the electron are recombined by large amount of holes at the on-state SCLT. Thus the NH_3 molecular is hardly desorpted from P3HT after removing the NH_3 gas result in the current doesn't back to the original current. Our other experiment presented the good recovering response at the off-state SCLT as shown in Fig. 4-11.

4.1.3 Nitric Oxide Sensing Results

In addition to study the sensor response to e-doping agents like NH_3, the response to hole doping agents is also investigated. Fig. 4-12 shows the real-time sensing response of J_{CE} to nitric oxide (NO). For NO sensing, the increased current of SCLT would accompany with the decrease of the on/off. Therefore, we chose the maximum on/off ratio (at Vce = -2.5 V) so that

we could explicitly show the on and off states during NO sensing. In opposite to the current-drop response to NH_3, the sensor exhibits a significant current increase when NO is injected into the sensing chamber. Since NO is known to serve as the hole doping agents on P3HT [45], it is suggested that hole concentrations in P3HT is increased and the hole current is also increases during NO sensing. The increased hole concentration in P3HT, however, deteriorates the switching function of SCLT. As shown in the shaded area (NO sensing area), off-state current increases significantly when SCLT is biased at V_{BE} = 0.9 V (off state). The poor base control over the channel potential may be due to the base-field shielding effect (or the screening effect) when P3HT is doped by hole-doping agents. Similar base-field shielding effects in SCLT have been observed in our previous reports when we added the tetrafluoro-tetracyano-quinodimethane (F4-TCNQ) to dope P3HT or when we irradiated light to create electron-hole pairs in P3HT or when we irradiated light to create electron-hole pairs in P3HT [46,47].

For the NO gas, the poor recovering behavior attribute to the good hole affinity of P3HT. The NO is converted into NO_2 and then the NO_2 capture the electron from P3HT to produce the hole [48]. Therefore, the excess hole increase the on-state current as well as the off-state current even removing the NO gas.

4.1.4 TCAD SILVACO ATLAS Simulation

After analyzing the experimental gas sensing response, TCAD SILVACO ATLAS

software is used to simulate the potential distribution in the vertical channel and the ideal transfer characteristics of SCLT. The simulation includes self-consistence of electron distributions and uniform doping distribution in the SCLT.

NH_3 Sensing Simulation

The influences of electron doping (e-doping) on SCLT are investigated to reflect the gas sensing response. Material parameters of TCAD simulation were defined in Ref.4.9. Figures 4-13(a) and 4-13(b) show 2-dimensional potential profiles of the vertical SCLT channel for e-doping concentrations of 10^{15} and 10^{16}, respectively. SCLT is biased in off state with V_{CE} = -1.2 V and V_{BE} = 1.5 V. It is observed that increasing e-doping concentration in P3HT results in the increase of the potential barrier, particularly in the central region of the vertical channel. The potential distributions along the central vertical channel of bottom and top injection structures with various e-doping concentrations are plotted in Fig. 4-14. For bottom injection, the potential distribution is from top Al (C) to bottom ITO (E); for top injection, it is from top Al/MoO_3 (E) to bottom ITO (C). From Fig. 4-14, the potential of both top and bottom injection structures increases with the increase of e-doping concentration. Although there are slight differences in the increase of potential with e-doping concentration as 10^{16} cm^{-3}, the reason why bottom injection structure exhibits better sensitivity to NH_3 is still unclear. cThe corresponding ideal J_{CE} - V_{BE} curves are shown in Fig. 4-15. With a fixed V_{CE} as -1.2 V, J_{CE}-V_{BE} curves shifts to the left when e-doping concentration increases,

indicating an increase of the potential barrier in the vertical channel. This simulation results agrees well with the sensing response for J_{CE}-V_{BE} described in Fig. 4-7. The current density variation ratios ($\triangle J/J_0$) as a function of V_{BE} for various doping concentrations are plotted shown in Fig. 4-16. The current density variation ratio ($\triangle J/J_0$), representing the response sensitivity, is defined as mentioned in Eq. 4.1-1, while J_{CE0} here is the collector current density at a electron doping concentration of 10^{15}. It was found that $\triangle J/J_0$ is strongly dependent on V_{BE} and the maximum $\triangle J/J_0$ is obtained in the switching region (e.g. 0.5 V < V_{BE} < 2 V in this case). As anticipated, the simulated results agree well with the experimental results in Fig. 4-8. As aforementioned, when SCLT is biased in the switching region, a slight change of base potential causes a significant current variation. The maximum $\triangle J/J_0$ in the switching region indicates that porous SCLT biased in the switching region exhibits largest response to e-doping as well as the gas molecule interaction.

NO Sensing Simulation

In addition to simulate the sensor response to e-doping agents like NH_3, the response to e-dedoping agents is also investigated. Material parameters of TCAD simulation were also defined in Ref.49. Figures 4-17(a) and 4-17(b) show 2-dimensional potential profiles of the vertical SCLT channel for e-dedoping concentrations of 10^{15} and 10^{16}, respectively. SCLT is biased in off state with V_{CE} = -1.2 V and V_{BE} = 0 V. It is observed that increasing e-dedoping concentration in P3HT results in the decrease of the potential barrier, particularly in the central

region of the vertical channel. The potential distributions along the central vertical channel from top Al (C) to bottom ITO (E) with various e-dedoping concentrations are plotted in Fig. 4-18. The corresponding ideal J_{CE} - V_{BE} curves are shown in Fig. 4-19. With a fixed V_{CE} as -1.2 V, J_{CE}-V_{BE} curves shifts to the right and J_{CE} continuously increases with e-dedoping concentration increases. Eventually, the J_{CE} becomes so high that the transistor cannot be turned off. This simulation results agrees well with the sensing response.

4.2 Amorphous IGZO TFT Hybrid Sensor

In this section, a concept of applying a-IGZO TFT on gas sensing by capping an inorganic sensing layer of metal-oxide semiconductor material ($W_{18}O_{49}$) is demonstrated. The test gases here are nitric oxide (NO) and ammonia (NH_3). The lowest detectable ammonia concentration is 50 ppb for tungsten oxide ($W_{18}O_{49}$) capped a-IGZO TFT hybrid sensor. Besides, 3-10 ppm nitric oxide gas sensing were also demonstrated.

Fig. 4-20 shows the transfer characteristics (I_{DS} -V_{GS}) of standard (STD) a-IGZO TFT and $W_{18}O_{49}$-capped a-IGZO TFT where V_{DS} is biased at 20 V. The channel length and width are 200 μm and 1000 μm respectively Parameters of a-IGZO TFT are shown in the inset of Fig. 4-20. It is observed that, with $W_{18}O_{49}$ capping, I_{DS} of a-IGZO TFT increases significantly and the transistor cannot be turned off. To solve this problem, we decrease the drain voltage so that the transistor can be turned off.

4.2.1 Ammonia Sensing Results

In our previous work, for STD a-IGZO TFT, no significant response can be found when ammonia concentration is 0.8 or 10 ppm [50]. The response of $W_{18}O_{49}$-capped a-IGZO TFT to ammonia is investigated. Drain current as a function of time is plotted in Fig. 4-21. The ammonia concentration here is 50-1000 ppm and the device is biased at $V_{DS} = V_{GS} = 3V$. Besides, the $W_{18}O_{49}$ is capped by spin coating. There is an obvious current drop when the device is exposed in ammonia. The sensing mechanism is supposed that ammonia molecules absorbed onto $W_{18}O_{49}$ act like reducing agents to inject electrons into $W_{18}O_{49}$ [51]. The negative potential on $W_{18}O_{49}$ layer, as the second gate, shifts the threshold voltage to be more positive and produces a current drop in a-IGZO TFT.

4.2.2 Nitric Oxide Sensing Results

To further verify the aforementioned mechanism, a typical oxidizing gas, NO, is used to stimulate the $W_{18}O_{49}$-capped device. In our previous work, when STD device is exposed to NO gas, a slow current drop is observed and the current drop is not able to be recovered even when NO is removed. Drain current as a function of time is plotted in Fig. 4-22, and $W_{18}O_{49}$ sensing layer here is formed by drop. The NO concentration is 3 to 10 ppm, the operating temperature is 80℃, and the device is biased at $V_{DS} = V_{GS} = 0.5V$. It is observed that the drain current increases when the device is exposed to NO and a recovery behavior is also obtained when NO is removed. The $W_{18}O_{49}$ capping blocks the reaction between NO and a-IGZO film.

The sensing behavior is dominated by the reaction between NO and $W_{18}O_{49}$ in which NO molecules act as oxidizing agents to withdraw electrons from $W_{18}O_{49}$ [51]. The positive potential on $W_{18}O_{49}$ film helps to turn on the transistor and thus increase the current of a-IGZO TFT.

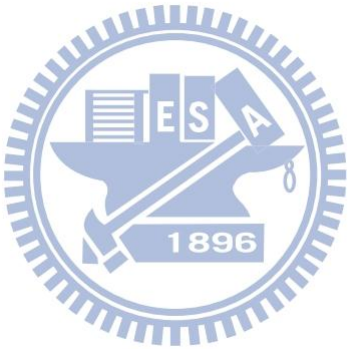

Figures of Chapter 4

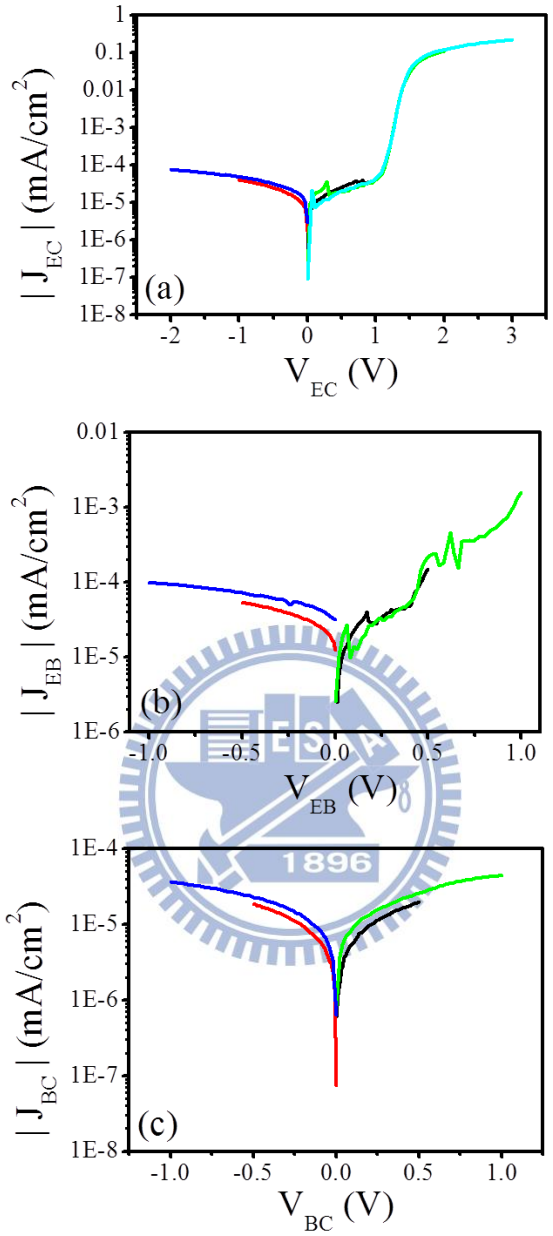

Fig. 4-1 The diode characteristics of porous SCLT, including EC, EB and BC diode. (a) EC diode characteristics between emitter and collector where emitter is biased and collector is grounded. (b) EB diode characteristics between emitter and base where emitter is biased and base is grounded. (c) BC diode characteristics between base and collector where base is biased and collector is grounded.

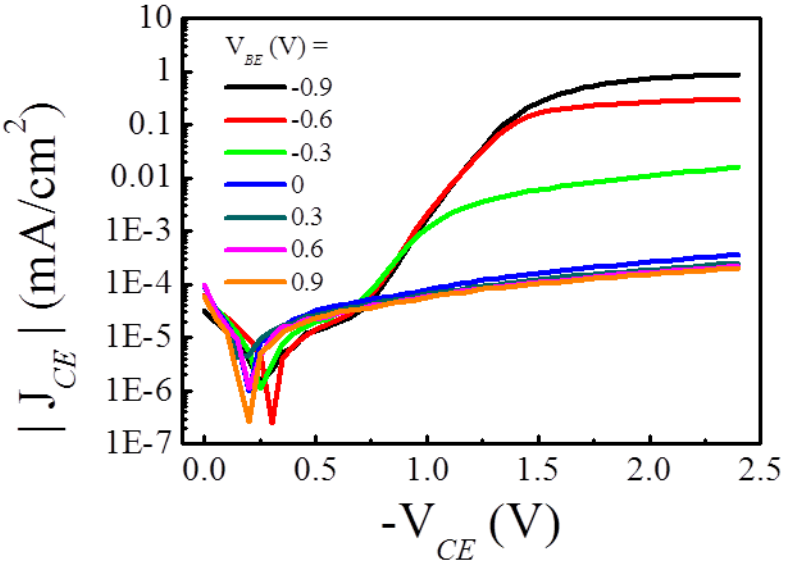

Fig.4-2 Output characteristics, the collector current density (J_{CE}) as a function of the collector voltage (V_{CE}), of the porous SCLT. With collector bias (V_{CE}) as -2.4 V and -1.2 V, porous SCLT exhibits an on/off current ratio as 4750 and 890, and a switching swing as 140 mV/dec. and 122 mV/dec., respectively.

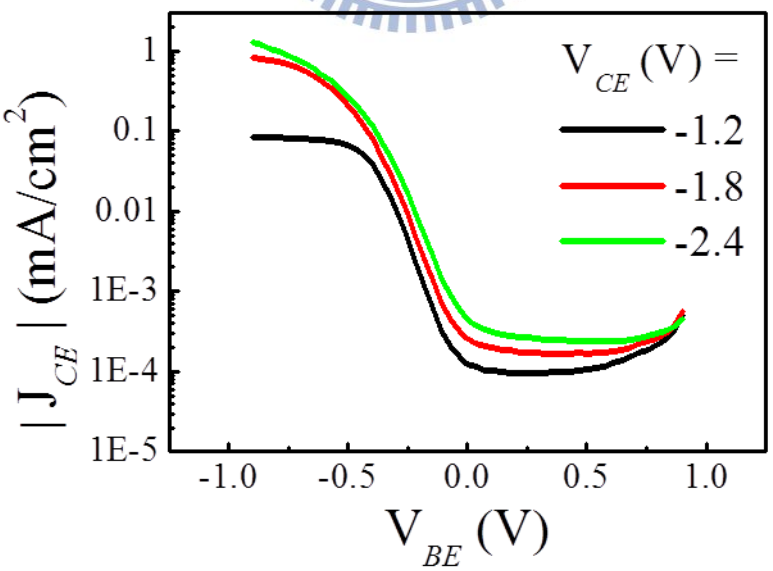

Fig.4-3 Transfer characteristics, the collector current density (J_{CE}) as a function of the base voltage (V_{BE}), of the porous SCLT.

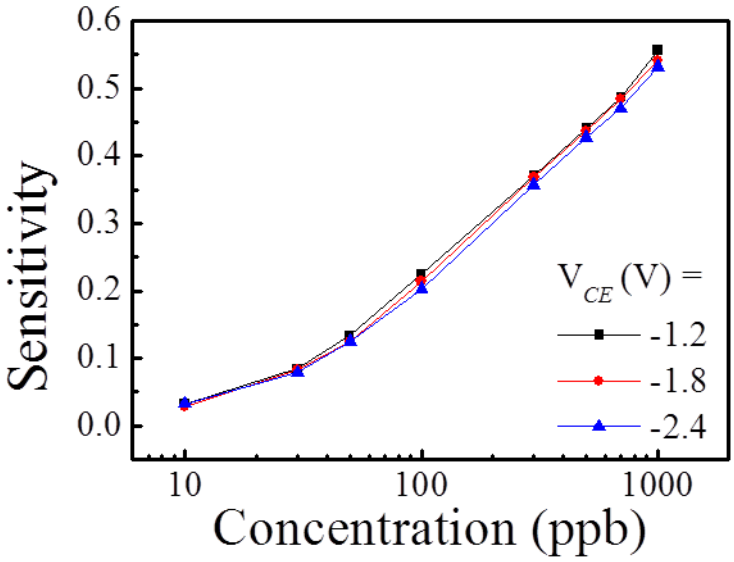

Fig. 4-4 A plot of sensitivity-NH_3 concentration with different V_{CE} bias conditions. The NH_3 concentrations were ranged from 30 ppb to 1000 ppb; the V_{CE} bias conditions are -1.2 V, -1.8 V and -2.4 V.

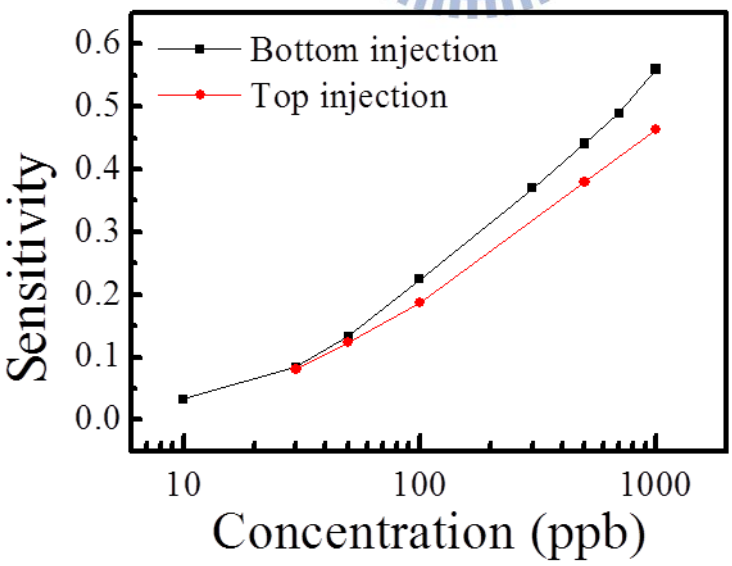

Fig. 4-5 A plot of sensitivity as a function of NH_3 concentration with different injection of holes.

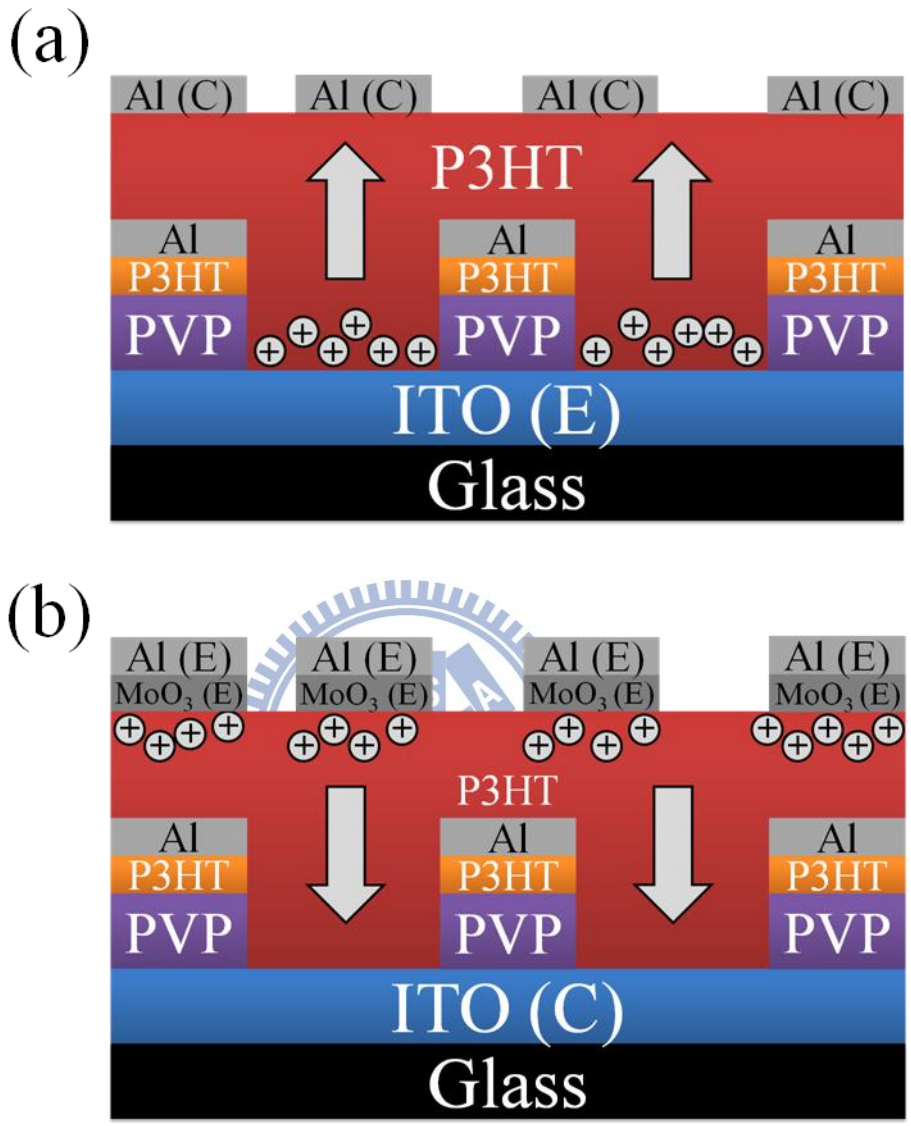

Fig. 4-6 Porous SCLT with different injection of holes. (a) Bottom injection of holes where ITO acts as emitter and Al acts as collector. (b) Top injection of holes where MoO_3/Al acts as emitter and ITO acts collector.

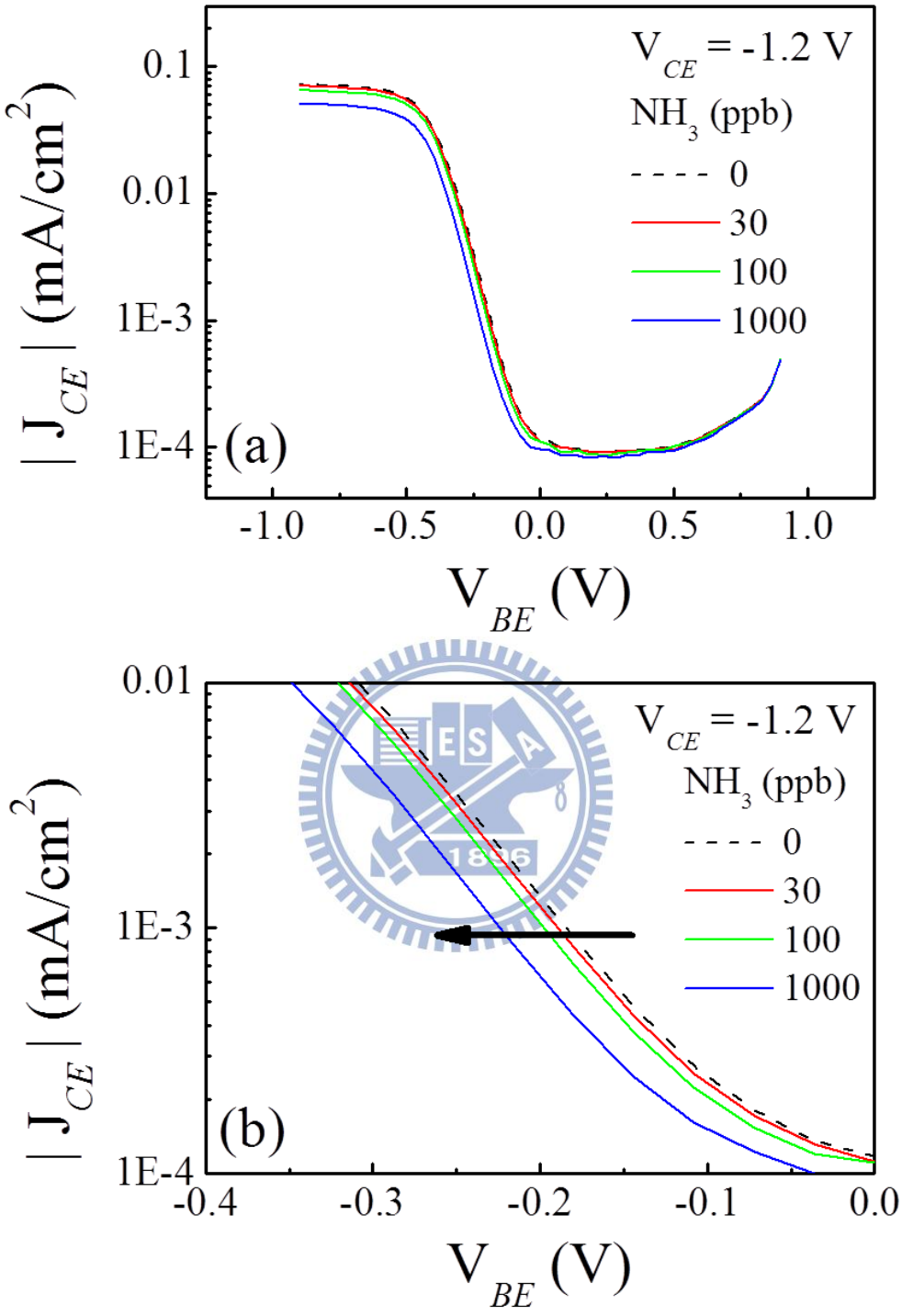

Fig. 4-7(a) A plot of J_{CE}-V_{BE}, representing the porous SCLT's sensing response to NH_3. V_{CE} was fixed as -1.2 V and the NH_3 concentrations were ranged from 30 ppb to 1000 ppb; (b) the response of the switching region (V_{BE} = -0.4 V to 0 V) of J_{CE}-V_{BE}.

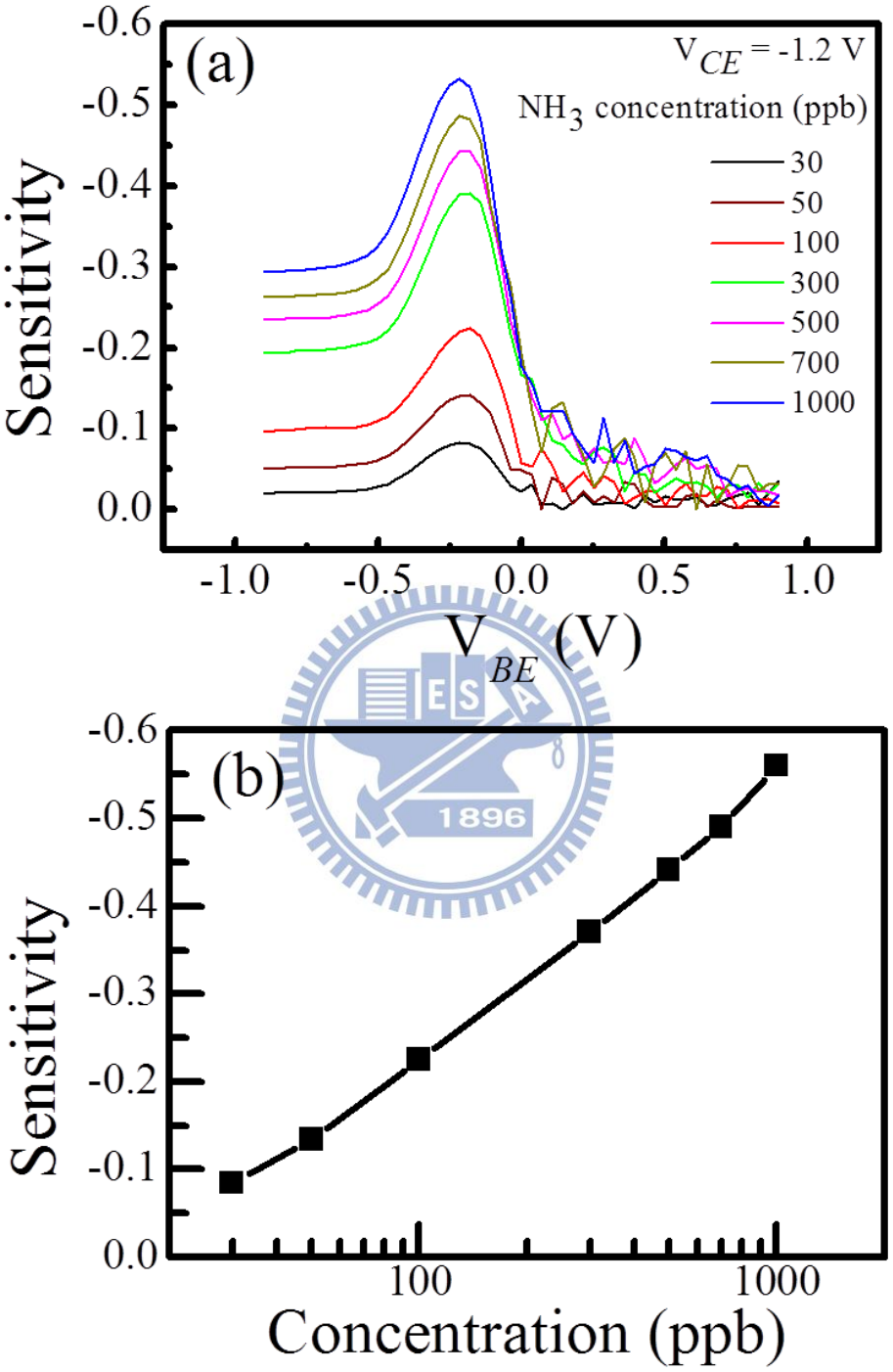

Fig. 4-8 The sensing sensitivities $\triangle J/J_0$ as a function of V_{BE} for various NH_3 concentrations; (b) Maximum sensitivity as a function of NH_3 concentration of SCLT sensor and diode sensor.

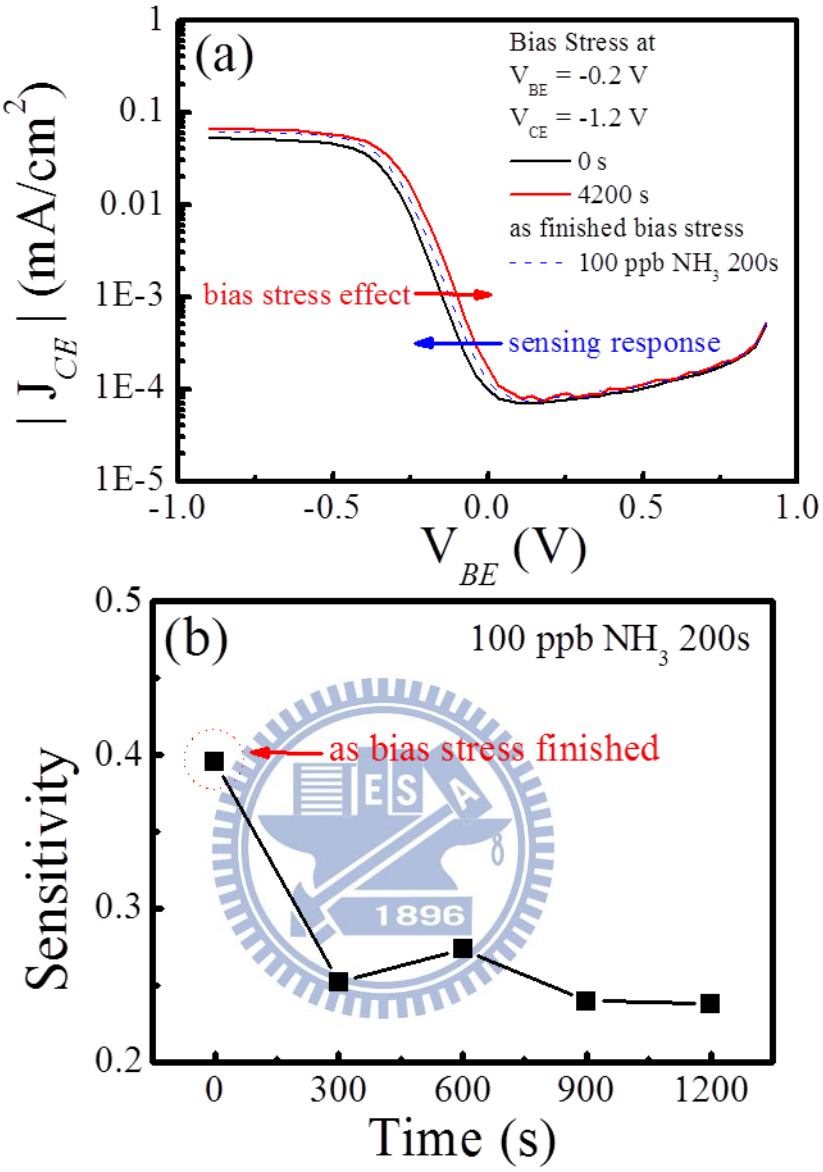

Fig. 4-9(a) Effects of bias stress and sensing response on J_{EC}-V_{BE} curve. Porous SCLT is bias as V_{BE} = -0.2 V and V_{CE} = -1.2 V and NH_3 concentration is 100ppb for 200 seconds. (b) Maximum sensitivity as function of the time after finishing of bias stress and NH_3 concentration is 100 ppb.

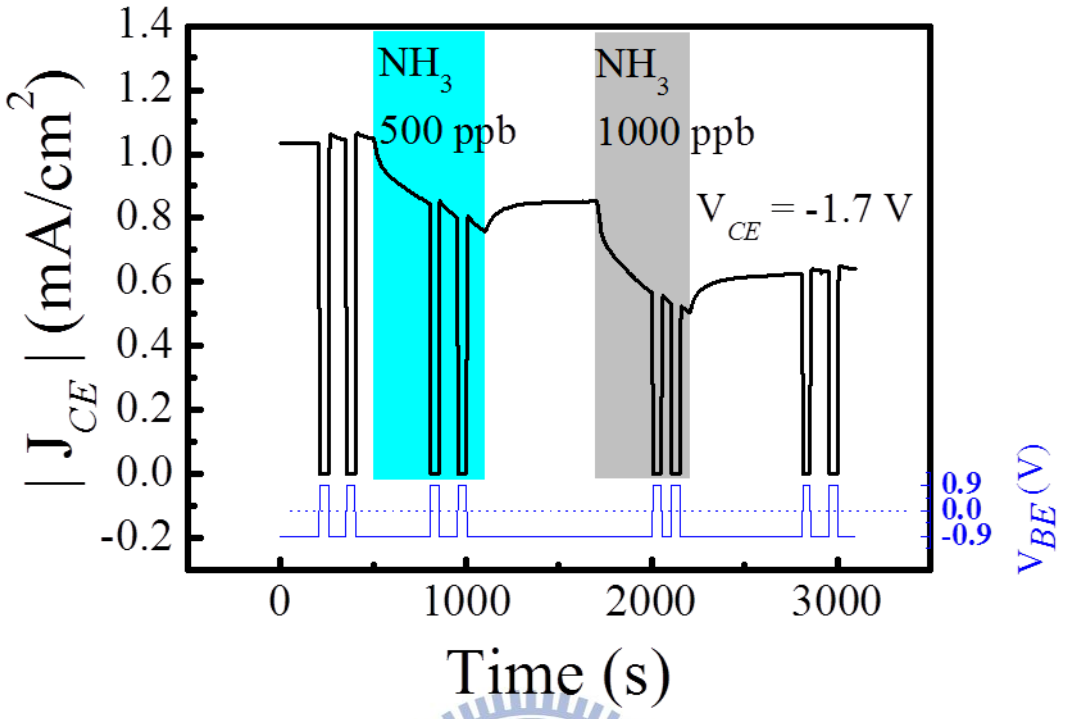

Fig. 4-10 The switching function of the porous SCLT under NH_3 sensing.

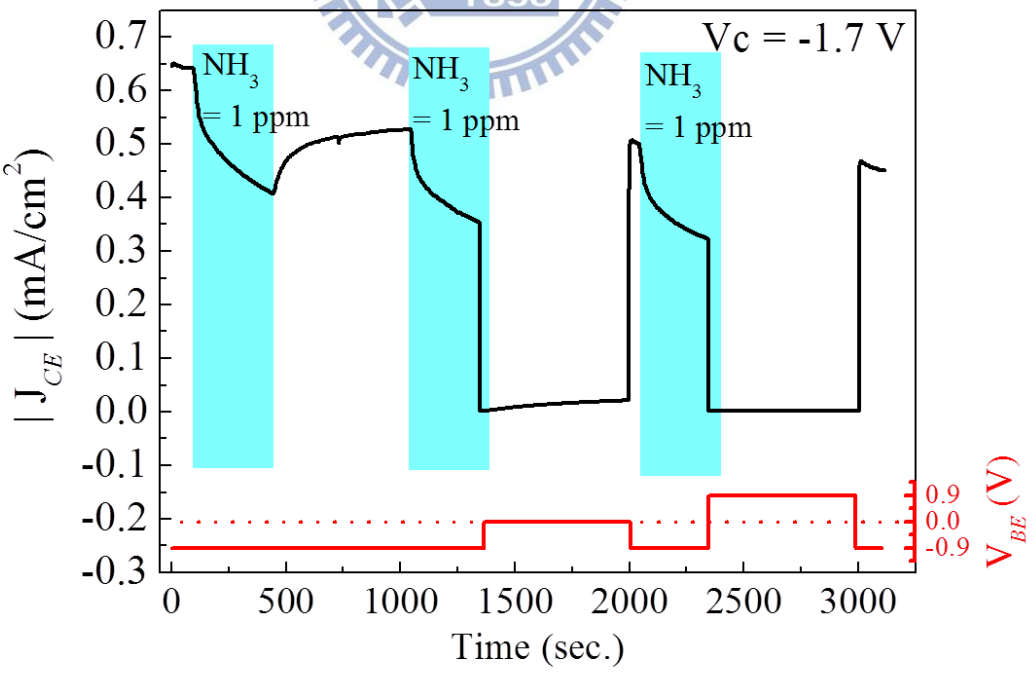

Fig. 4-11 The real-time NH_3 recovering response at V_{BE} = -0.9 V, 0 V and 0.9 V.

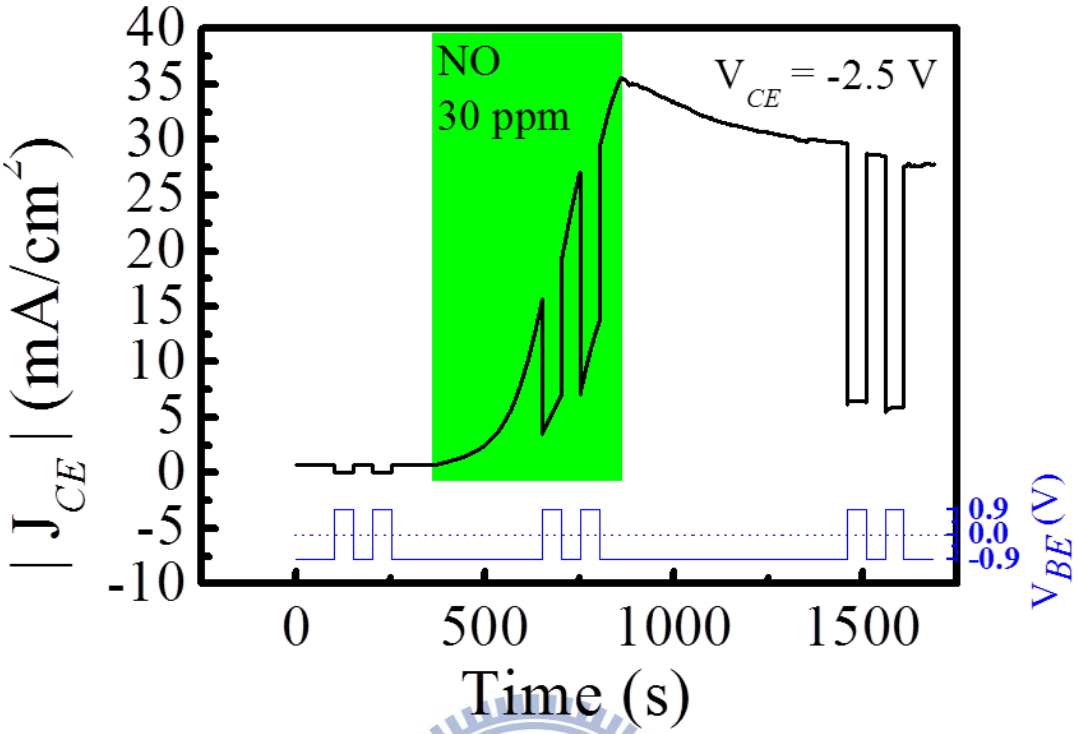

Fig. 4-12 The real-time sensing response of J_{CE} to nitric oxide (NO).

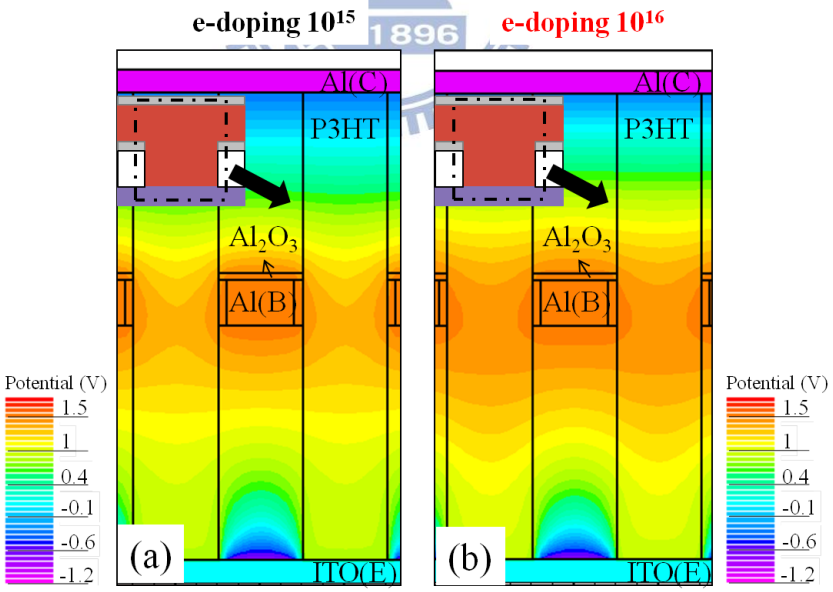

Fig. 4-13 2-dimensional potential profiles of the vertical SCLT channel for e-doping concentrations. (a) e-doping concentrations of 10^{15}. (b) e-doping concentrations of 10^{16}. SCLT is biased in off state with V_{CE} = -1.2 V and V_{BE} = 1.5 V.

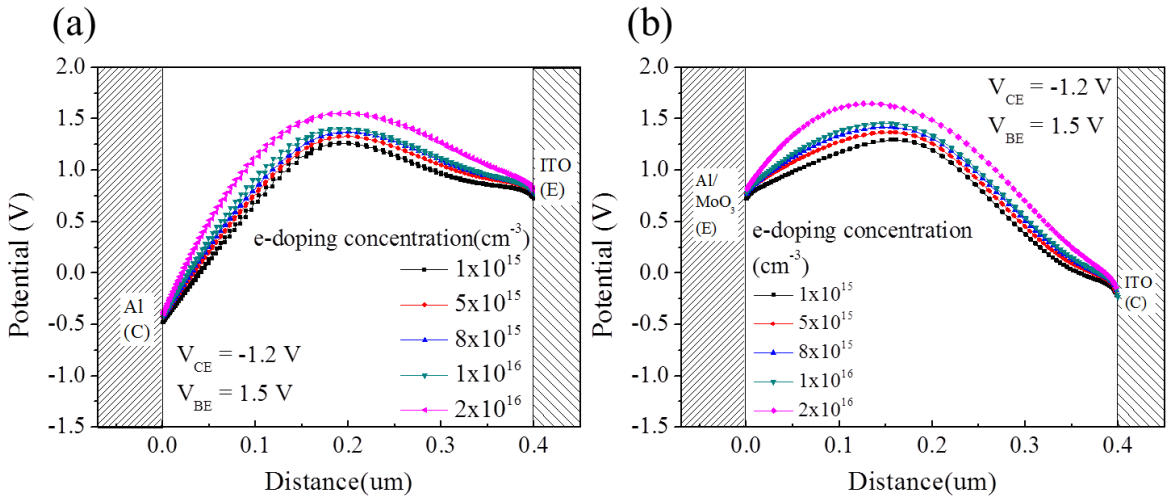

Fig. 4-14 The potential distributions along the central vertical channel with various e-doping concentrations. (a) Top injection: from top Al (C) to bottom ITO (E); (b) bottom injection: from top Al/MoO_3 (E) to bottom ITO (C).

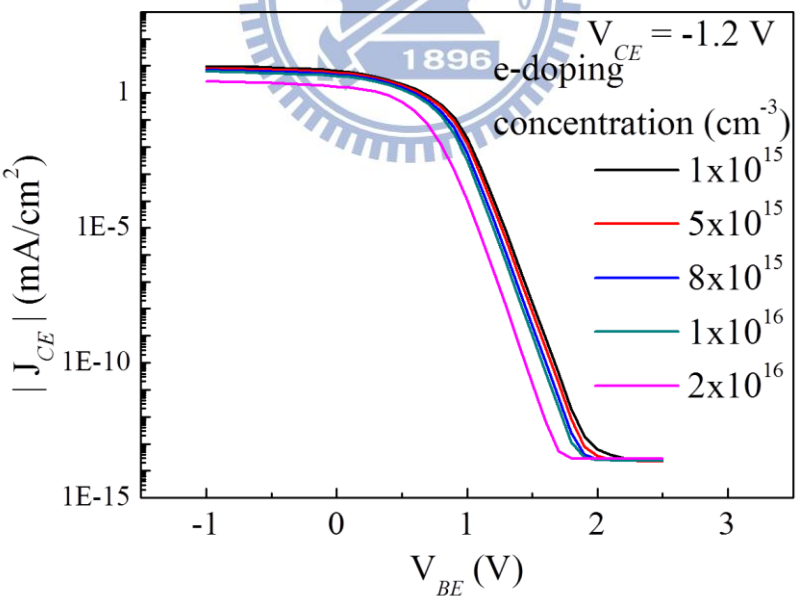

Fig.4-15 The corresponding ideal J_{CE} - V_{BE} curves.

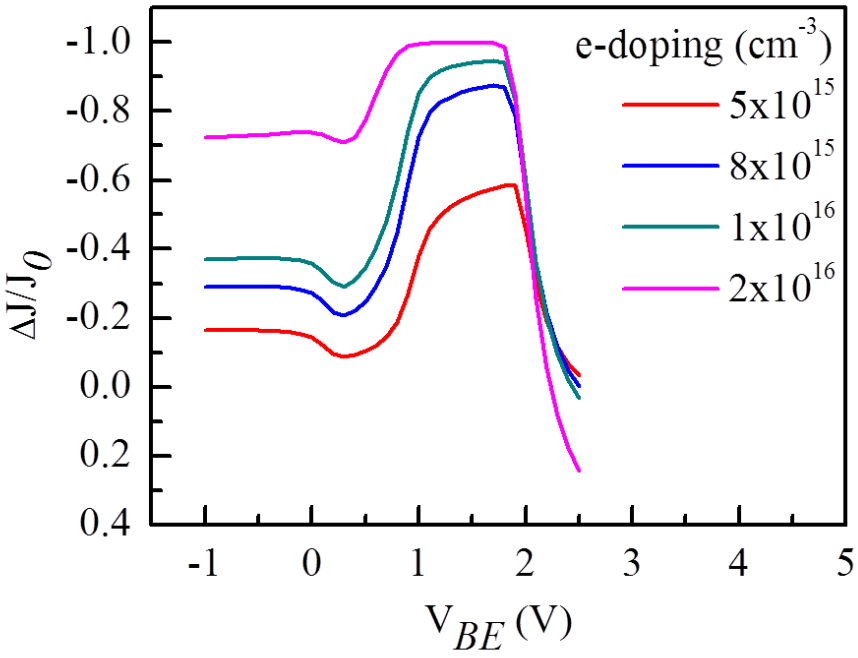

Fig. 4-16 The current density variation ratios ($\triangle J/J_0$) as a function of V_{BE} for various doping concentrations.

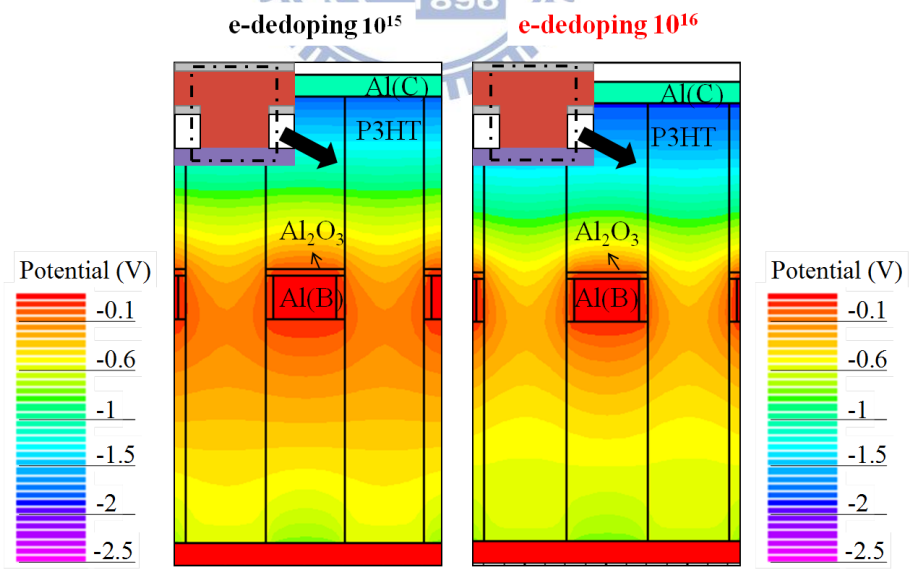

Fig. 4-17 2-dimensional potential profiles of the vertical SCLT channel for e-dedoping concentrations. (a) e-dedoping concentrations of 10^{15}. (b) e-dedoping concentrations of 10^{16}. SCLT is biased in off state with V_{CE} = -1.2 V and V_{BE} = 0 V.

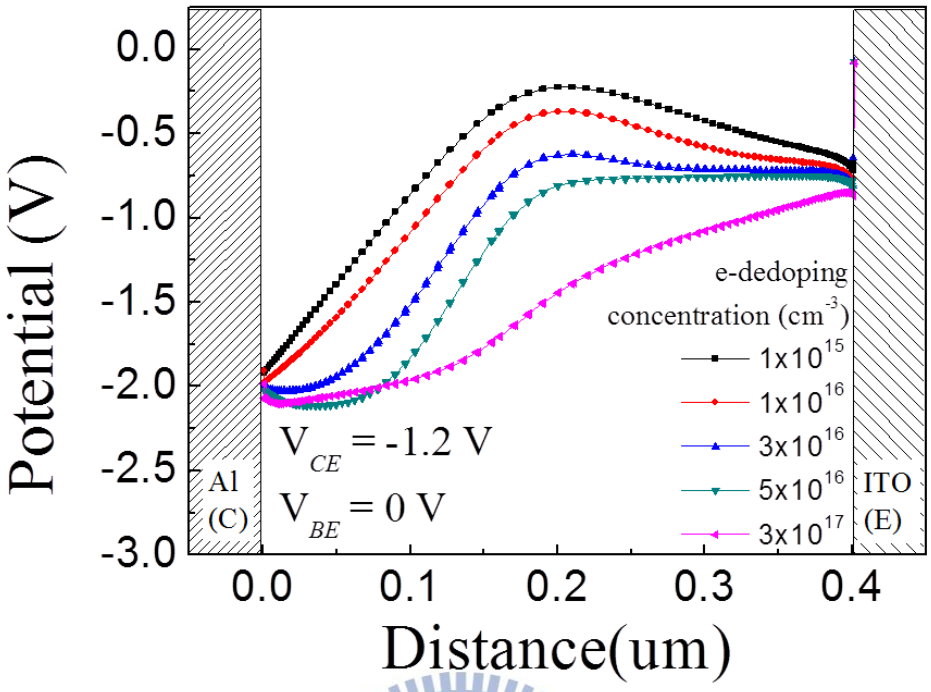

Fig. 4-18 The potential distributions along the central vertical channel from top Al (C) to bottom ITO (E) with various e-dedoping concentrations.

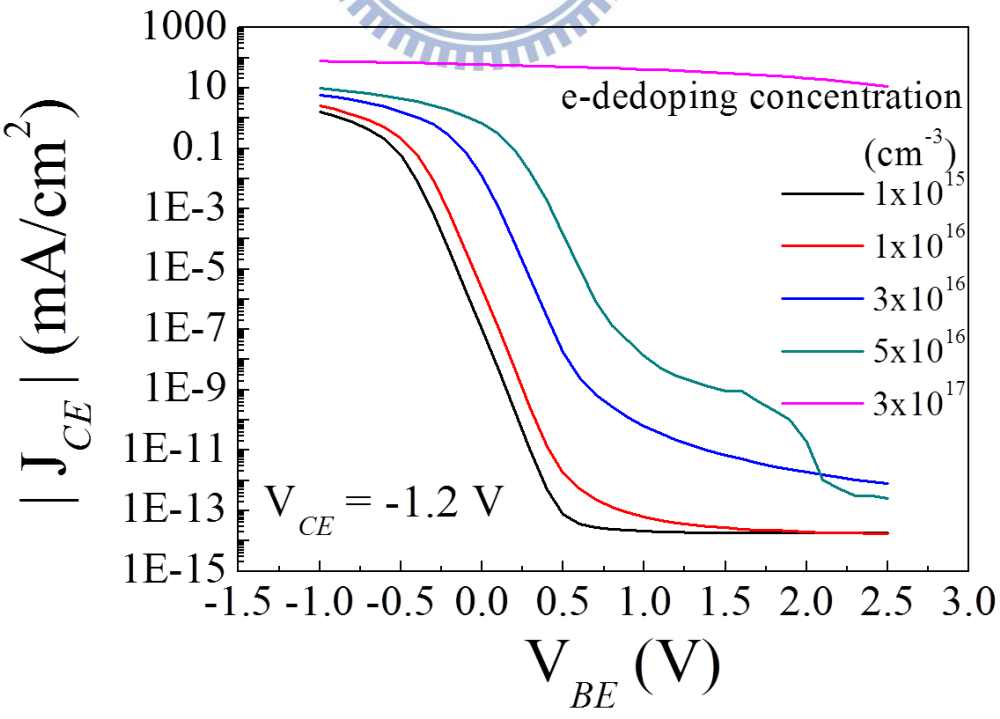

Fig.4-19 The ideal J_{CE} - V_{BE} curves.

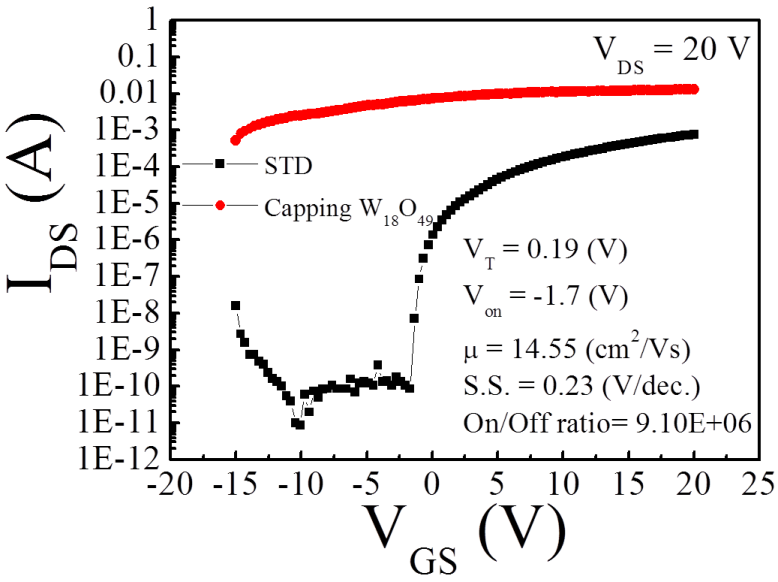

Fig.4-20 Transfer characteristic of STD a-IGZO TFT and $W_{18}O_{49}$-capped a-IGZO TFT. The channel length and width are 200 μm and 1000 μm respectively. Parameters of a-IGZO TFT are shown in the inset of Fig. 4-20.

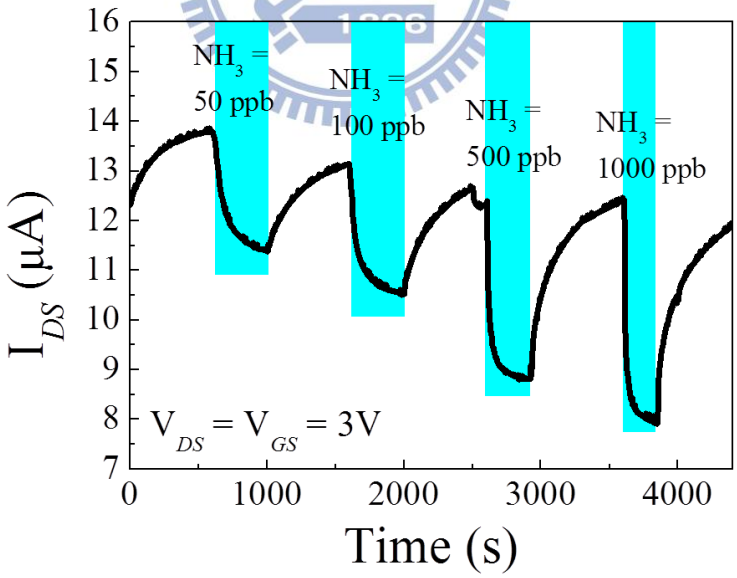

Fig. 4-21 Drain current as a function of time. The ammonia concentration here is 50-1000 ppm and the device is biased at V_{DS} = V_{GS} = 3V. Besides, the $W_{18}O_{49}$ is capped by spin coating.

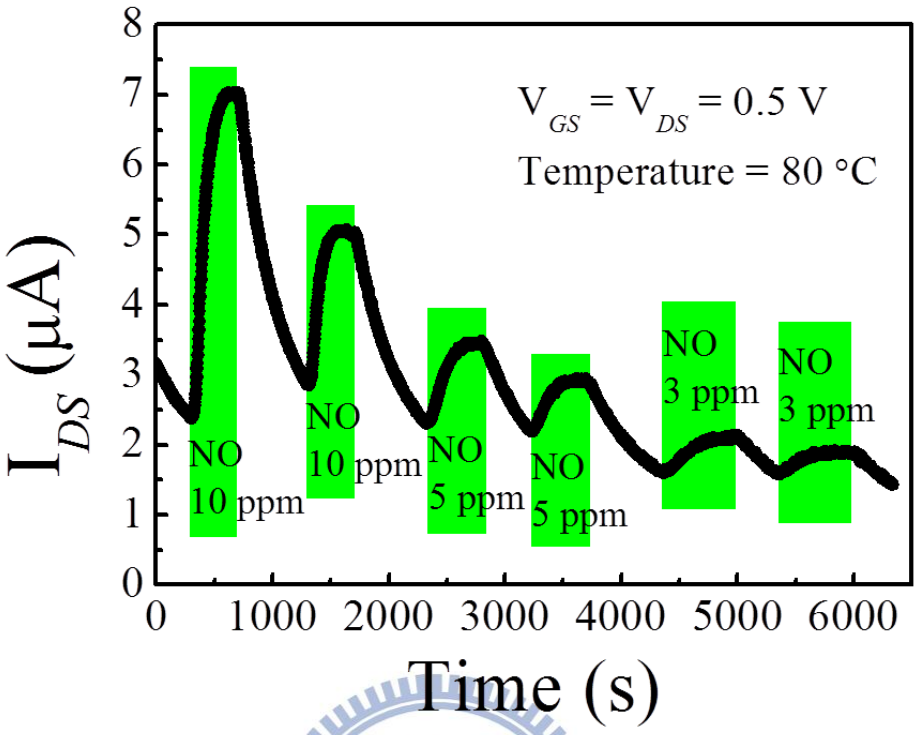

Fig. 4-22 Drain current as a function of time is plotted in and $W_{18}O_{49}$ sensing layer here is formed by drop. The NO concentration is 3 to 10 ppm, the operating temperature is 80℃, and the device is biased at $V_{DS} = V_{GS} = 0.5$ V.

Chapter 5 Conclusion and Future Work

5.1 Conclusion

We proposed a low-power sensitive gas sensor embedded in a vertical polymer transistor, SCLT. In SCLT, current flows in the bulk region of the vertical channel. Exposing the vertical channel to gas molecules creates a significant interaction between channel and gas molecules and hence a high gas sensitivity. Moreover, the potential profile in the vertical channel is sensitive to the channel doping concentration as well as the base bias. When P3HT-based porous SCLT is biased in the switching region, a maximum sensitivity to NH_3 can be obtained with a detection limit as 30 ppb. The sensitivity is much higher than P3HT-based OTFT, which has a NH_3 detection limit higher than 1 ppm. The high NH_3 sensitivity achieved in this work facilitates the development of non-invasive breath ammonia analysis for point-of-care applications. The proposed sensor integrating a gas sensor and a switching transistor in one single device also can be used as pixel circuitry in sensor array applications. On the other hand, we demonstrated a gas sensor based on inorganic a-IGZO TFTs and sensing layer. The tungsten oxide ($W_{18}O_{49}$) as sensing layer is capped onto the back channel of a conventional bottom-gate top-contact a-IGZO TFT. When the sensing layer contacts with oxidizing or reducing gas molecules, charge transfer between the sensing layer and the gas molecules changes the potential of the sensing layer. The variation in the sensing layer potential can be detected by the underlying a-IGZO TFT since the sensing layer is served as a floating second

gate. The lowest detectable NH_3 and NO concentrations are 50 ppb and 3 ppm respectively.

5.2 Future Work

For SCLT gas sensor, although the limit of detection is enough for gas test of human breath, we still hope to further decrease detectable concentration and increase the response. Besides, we will also try to cooperate with doctors to apply SCLT sensor to mice experiment so that one day our SCLT sensor can be used as clinic diagnosis. In addition, the SCLT sensor integrating a gas sensor and a switching transistor in one single device can be applied to pixel circuitry in sensor array applications. With the novel ideal, one day there might be a disposable and highly sensitivity ammonia sensor so that could be used in clinic diagnosis.

On the other hand, the concept of integrating metal oxide semiconductor as sensing layer and a-IGZO TFTs is verified by our a-IGZO TFT hybrid sensor. However, the sensing response is not high enough. To further enhance the response, we will try different morphologies of tungsten oxide and different metal oxide materials. We hope that one day the hybrid sensor could become a real-time and highly sensitive toxic gas sensor.

Appendix

A.1 Effective Mobility Enhancement Induced by Femtosecond Laser Irradiation in a-IGZO TFT

A.1.1 Abstract

A preliminary result of femtosecond laser irradiation (FLI) on a-IGZO TFTs is demonstrated in this appendix. A high mobility top-gate (TG) a-IGZO thin film transistor (TFT) is proposed. It is supposed that femtosecond laser irradiation (FLI) on a-IGZO film induces the increase of channel conductivity and forms a high field-effect mobility (~84 cm^2/Vs) TG a-IGZO TFT.

A.1.2 Motivation

It is proposed that the local conductivity of indium tin oxide (ITO) films is significant enhanced due to the formation of self-organized nanodots induced by femotosecond laser pulses [52]. In addition, a high mobility (~79cm^2/Vs) a-IGZO TFT with nano-dots doping (NDD) was proposed in our previous work [53]. In that work, the channel of devices is treated with Ar plasma to form NDD and as a result the field-effect mobility is enhanced. We can find the aforementioned concepts of nano-dots are similar. As a result, in this study, we use femtosecond laser to irradiate the channel of as-deposited a-IGZO film to enhance the mobility. The femtosecond laser used here is a Ti:sapphire laser (Legend USP, Coherent) with 800 nm wavelength and 100 fs pulse duration.

A.1.3 Device Fabrication

In this section, fabrication of the performance-enhanced a-IGZO TFTs with femtosecond laser irradiation is demonstrated. The a-IGZO TFTs here are top contact with dual gates (DG). The fabrication processes of FLI in the beginning part including gate dielectric layer, substrate cleaning, and a-IGZO film deposition are similar to section 3.3 a-IGZO TFTs hybrid sensor except for the thickness of a-IGZO film and $O_2/(Ar+O_2)$ ratio during rf sputter. Thickness of a-IGZO film and $O_2/(Ar+O_2)$ ratio during rf sputtering a-IGZO film are 20 nm and 0%. Two-dimensional high mobility DG a-IGZO TFT is showed in Fig. A-1.

The channel length of both TG and bottom-gate (BG) is defined as the length of TG electrode. Because the a-IGZO film except for the region covered with TG electrode is treated with Ar plasma, a-IGZO surface treated with Ar plasma becomes highly conductive so that the bare channel region can be regarded as extension of S/D electrodes.

With a-IGZO film deposited on 100 nm SiNx basing on heavily p-doped Si substrate, the fabrication processes are as follows. First, the as-deposited a-IGZO film was irradiated by femtosecond laser. Second, use 8 wt% PVP solution dissolved in PGMEA within which PVP: PMF = 11: 4 as mentioned in step (4) of section 3.2 to form a 200 nm PVP layer on a-IGZO film as TG insulator layer, and anneal at 200℃ for 1 hour in air. Third, 100 nm Al was deposited on PVP using shadow masks by thermal evaporation at the rate of 0.2 nm/s. The 100 nm Al was regarded as TG electrode and hard mask for O_2 plasma. Fourth, use O_2 plasma at

50W for 12.5 minutes to remove the PVP without the coverage of Al and then 50W Ar plasma was used to treat a-IGZO surface for 30 second. Finally, 40 nm Al was deposited as source/drain electrodes using shadow masks by thermal evaporator at the rate of 0.2 nm/s. The flowchart of the fabrication processes is showed in. Fig. A-2.

A.1.4 Results and Discussion

Fig. A-3 shows the transfer characteristics of a-IGZO TFT with FLI. The parameters of a-IGZO TFT and the condition of FLI are shown in Table A-1. It is observed the effective field-effect mobility of TG a-IGZO is enhanced, while that of BG a-IGZO is not improved. The supposed reason for the enhancement of TG device is that there are nano-dots formed on the channel as proposed in ITO surface [52]. With nano-dots, the carrier concentration in channel is increase resulting the enhancement of mobility.

A.1.5 Conclusion and Future Work

(1) Conclusion

A high mobility (~84 cm^2/Vs) a-IGZO TFT is proposed due to the femtosecond laser irradiation on as-deposited a-IGZO film. It is supposed there is formation of nano-dots on the channel resulting in the increase of carrier concentration, and therefore the mobility is enhanced.

(2) Future work

The study of the effects of FL irradiation on a-IGZO TFT is still in preliminary stage. SEM images should be taken to verify whether there is formation of nano-dots or not. In addition, the relation between irradiation power/time of FL and mobility is still unknown and needs to be figured out. Besides, the stability of a-IGZO TFT with FL irradiation is also a important issue to study. In a word, it seems that FL irradiation does help a-IGZO TFT to improve the mobility, and an excellent performance of a-IGZO TFT can be expected by modulating FL irradiation.

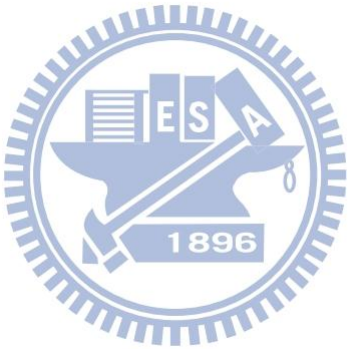

Figures of Appendix

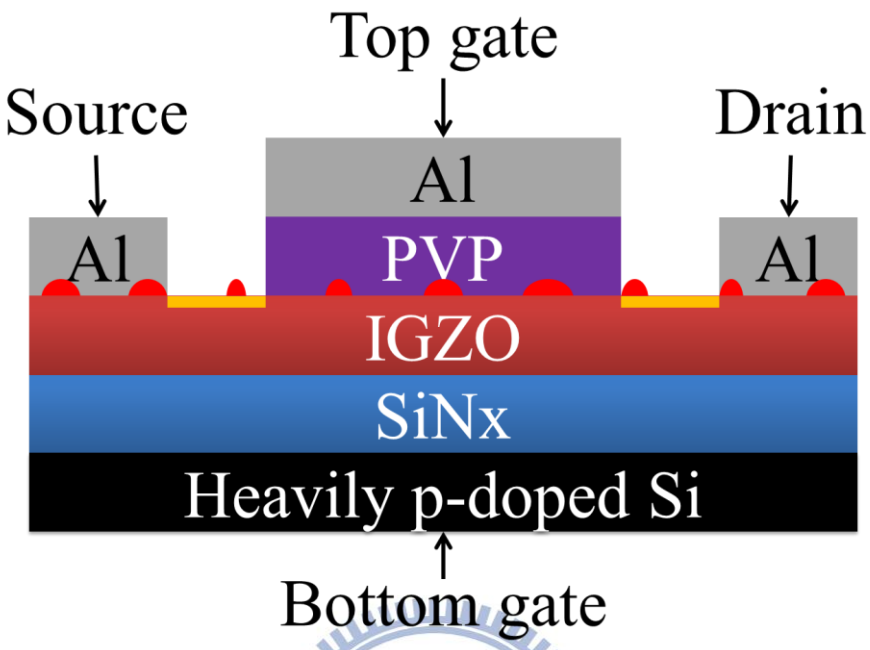

Fig. A-1 Two-dimensional performance enhanced DG a-IGZO TFT .

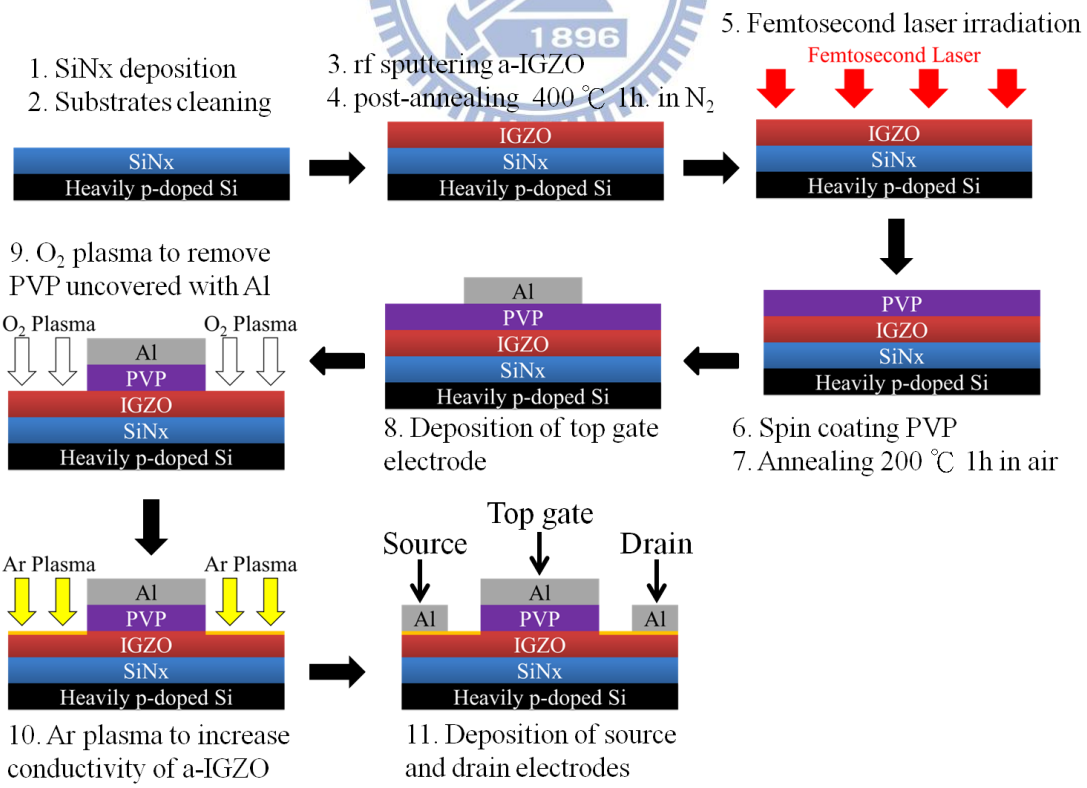

Fig. A-2 The flowchart of the fabrication processes.

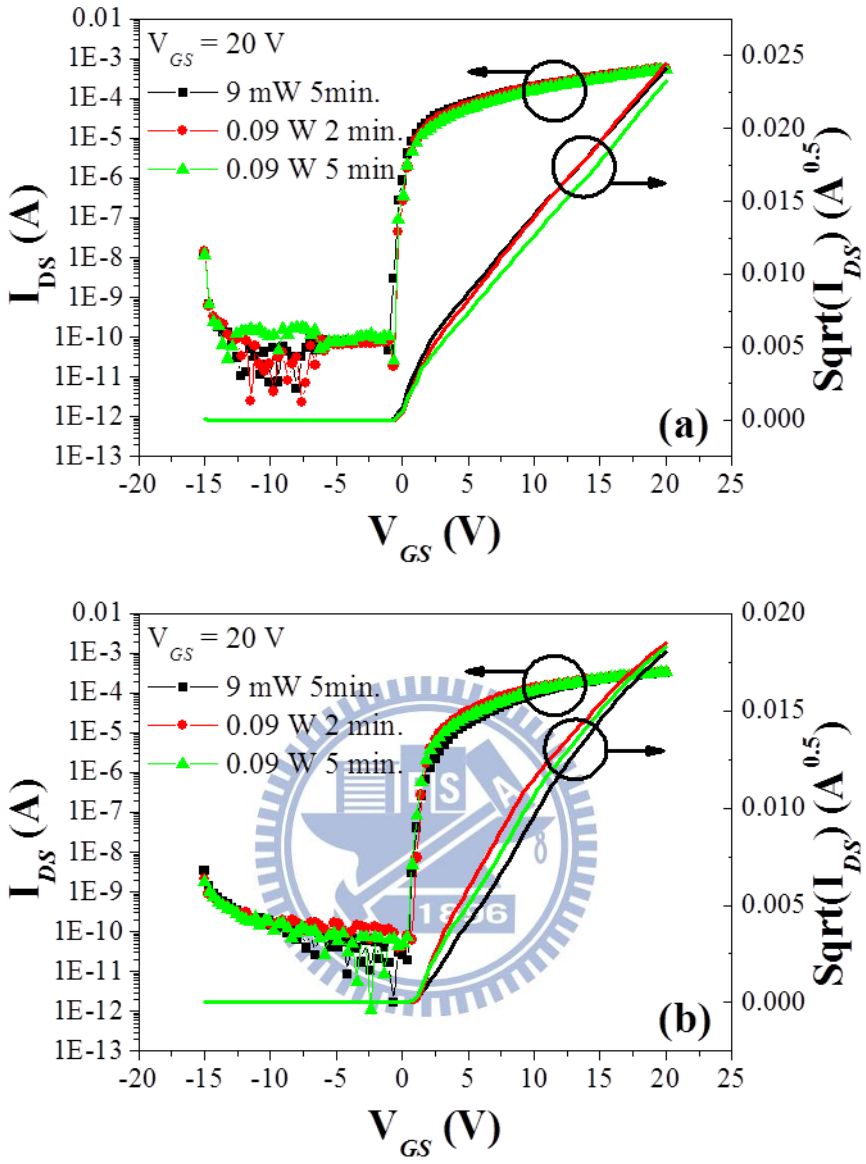

Fig. A-3 The transfer characteristics of a-IGZO TFT with FLI. (a) Bottom gate. (b) Top gate.

Device	Condition	C (nF/cm^2)	Length (μm)	V_T (V)	V_{on} (V)	μ (cm^2/Vs)	S.S. (V/dec.)	On/Off Ratio
Bottom Gate	9 mW, 5 min.	53.1	567	-3.4	-1	23.03	0.19	1.20E+07
	0.09 W, 2min.		366	-2.47	-0.65	16.81	0.1	3.20E+07
	0.09 W, 5 min.		372	-2.06	-0.65	15.36	0.1	2.10E+07
Top Gate	9 mW, 5 min.	16	567	1.29	0.4	86.45	0.16	1.70E+07
	0.09 W, 2min.		366	0.27	0.75	68.35	0.19	5.40E+06
	0.09 W, 5 min.		372	0.49	0.4	58.42	0.19	4.60E+06

Table A-1 The parameters of a-IGZO TFT and the condition of FLI.

References

[1] K. M. Coakly and M. D. McGehee, Chem. Mater. **16**, 4533 (2004).

[2] H. Sirringhaus, P. J. Brown, R. H. Friend, M. M. Nielsen, K. Bechgaard, B. M. W. Langeveld-Voss, A. J. H. Spiering. R. A. J. Janssen, E. W. Meijer, P. Herwig, D. M. de Leeuw, Nature **401**, 685 (1999).

[3] H. Sirringhaus, P. J. Brown, R. H. Friend, M. M. Nielsen, K. Bechgaard, B. M. W. Langeveld-Voss, A. J. H. Spiering. R. A. J. Janssen, E. W. Meijer, Synth. Met. **111-112**, 129 (2000).

[4] D. H. Kim, Y. D. Park, Y. Jang, H. Yang, Y. H. Kim, J. I. Han, D. G. Moon, S. Park, T. Chang, C. Chang, M. Joo, C. Y. Ryu, and K. Cho, Adv. Fun. Mat. **15**, 77 (2005).

[5] Y. C. Chao, W. W. Tsai, C. Y. Chen, H. W. Zan, H. F. Meng, S. L. Jiang, C. M. Chiang, and M. C. Ku, IEEE International Electron Device Meeting, (2009).

[6] G. Eranna, B. C. Joshi, D. P. Runthala, and R. P. Gupta, Crit. Rev. Solid State Mater. Sci. **29**, 111 (2004).

[7] G. N. Chaudhari, A. M. Bende, A. B. Bodade, S. S. Patil, and V. S. Sapkal, Sens. Actuators B **115**, 297 (2006).

[8] B. Timmer, W. Olthuis, and A. Berg, Sens. Actuators B **107**, 666 (2005).

[9] G. Korotcenkov, I. Blinov, M. Ivanov, J.R. Stetter, Sens. Actuators B **120**, 679 (2007).

[10] Y. K. Chung, M. H. Kim, W. S. Um, H. S. Lee, J. K. S. Song, Ch. Choi, K. M. Yi, M. J.

Lee, and K. W. Chung, Sens. Actuators B **60**, 49 (1999).

[11] Y. B. Shen, T. Yamazaki, Z. F. Liu, D. Meng, T. Kikuta, and N. Nakatani, Thin Solid Films **517**, 2069 (2009).

[12] J. Pollleux, A. Gurlo, N. Barsan, U. Weimar, M. Antonietti, and M. Niederberger, Angew. Chem. Int. Ed. **118**, 267 (2006).

[13] Y. G. Choi, G. Sakai, K. Shimanoe, and N. Yamazoe, Sens. Actuators B **101**, 107 (2004).

[14] M. Oritay, H. Ohta, M.Hirano, S. Narushima, and H. Hosono, Philosophical magazine B **81**, 501 (2001).

[15] H. Yabuta, M. Sano, K. Abe, T. Aiba, T. Den, H. Kumomi, K. Nomura, T. Kamiya, and H. Hosono, Appl. Phys. Lett. **89**, 112123 (2006).

[16] A. Tsukazaki, A. Ohtomo, T. Onuma, M. Ohtani, T. Makino, M. Sumiya, K. Ohtani, S. F. Chichibu, S. Fuke, Y. Segawa, H. Ohno, H. Koinuma, and M. Kawasaki, Nature Mater. **4,** 42 (2005).

[17] Y. Sun and J. A. Rogers, Adv. Mater. **19**, 1897 (2007).

[18] H. Kumomi, K. Nomura, T. Kamiya, and H. Hosono, Thin Solid Films **516**, 1516 (2008).

[19] H. Hosono, K. Nomura, Y. Ogo, T. Uruga, and T. Kamiya, J. Non-Cryst. Solids **354**, 2796 (2008).

[20] W. B. Jackson, R. L. Hoffman, G. S. Herman, Appl. Phys. Lett. **87**, 193503 (2005).

[21] P. Görrn, M. Sander, J. Meyer, M. Kröger, E. Becker, H. H. Johannes, W. Kowalsky, and T.

Riedl, Adv. Mater. **18**, 738 (2006).

[22] W. Lim, D. P. Norton, J. H. Jang, V. Craciun, S. J. Pearton, and F. Ren, Appl. Phys. Lett. **92**, 122102 (2008).

[23] R. L. Hoffman, B. J. Norris, and J. F. Wager, Appl. Phys. Lett. **82**, 733 (2003).

[24] H. Q. Chiang, B. R. McFarlane, D. Hong, R. E. Presley, and J. F. Wager, J. Non-Cryst. Solids **354**, 2826 (2008)

[25] K. Nomura, H. Ohta, A. Takagi, T. Kamiya, M. Hirano, and H. Hosono, Nature **432**, 488 (2004).

[26] H. H. Hsieh, H. H. Lu, H. C. Ting, C. S. Chuang, C. Y. Chen, and Y. Lin, J. Inf. Disp. **11**, 160 (2010).

[27] J. S. Park, T. W. Kim, D. Stryakhilev, J. S. Lee, S. G. An, Y. S. Pyo, D. B. Lee, Y. G. Mo, D. U. Jin, and H. K. Chung, Appl. Phys. Lett. **95**, 013503 (2009).

[28] C. Shimamoto, I. Hirata, and K. Katsu, Hepato-Gastroenterology **47**, 443 (2000).

[29] M. Righettoni, A. Tricoli, and S. E. Pratsinis, Anal. Chem. **82**, 3581 (2010).

[30] J. Shi, G. Hu, Y. Sun, M. Geng, J. Wu, Y. Liu, M. Ge, J. Tao, M. Cao, and N. Dai, Sens. Actuators B **156**, 820 (2011).

[31] H. W. Zan, W. T. Chen, C. C. Yeh, H. W. Hsueh, C. C. Tsai, and H. F. Meng, Appl. Phys. Lett. **98**, 153506 (2011).

[32] N. F. Mott and D. Gurney, Electronic Processes in Ionic Crystals, Oxford.

[33] A. Takagi, K. Nomura, H. Ohta, H. Yanagia, T. Kamiya, M. Hirano, and H. Hosono, Thin Solid Films **486**, 38 (2005)

[34] K. Nomura, T. Kamiya, H. Ohta, K. Ueda, M. Hirano, and H. Hosono, Appl. Phys. Lett. **85**, 1993 (2004).

[35] P. Barquinha, L. Pereira, G. Gonçalves, R. Martins, and E. Fortunato, Journal of The Electrochemical Society **156**, 161 (2009).

[36] T. Kamiya, H. Hiramatsu, K. Nomura, and H. Hosono, J. Electroceram. **17**, 267 (2006).

[37] H. Hosono, J. Non-Cryst Solids **352**, 851 (2006).

[38] H. C. Pan, M. H. Shiao, C. Y. Su, and C. N. Hsiao, J. Vac. Sci. Technol. **23**, 1187 (2005).

[39] R. Martins, P. Barquinha, I. Ferreira, L. Pereira, G. Goncalves, and E. Fortunato, J. Appl. Phys. **101,** 044505 (2007).

[40] K. Nomura, A. Takagi, T. Kamiya, H. Ohta, M. Hirano, and H. Hosono, J. J. Appl. Phys. **4**5, 4303(2006).

[41] J. W. Jeong, Y. D. Lee, Y. M. Kim, Y. W. Park, J. H. Choi, T. H. Park, C. D. Soo, S. M. Won, I. K. Han, and B. K. Ju, Sens. Actuator B **146**, 40 (2010).

[42] T. Hibbard, and A. J. Killard, Crit. Rev. Anal. Chem. **41,** 21 (2011).

[43] H. Bai, and G. Shi, Sensors **7**, 267 (2007)

[44] B. Guo, A. Bermak, P. C. H. Chan, and G. Z. Yan, Solid-State Electro. **51**, 69 (2007).

[45] V. Saxena, D. K. Aswal, M. Kaur, S. P. Koiry, S. K. Gupta, J. V. Yakhmi, R. J. Kshirsagar,

and S. K. Deshpande, Appl. Phys. Lett. **90**, 043516 (2007).

[46] Y. C. Chao, C. Y. Chen, H. W. Zan, and H. F. Meng, J. Phys. D: Appl. Phys. **43,** 205101 (2010).

[47] H. W. Zan, W. W. Tsai, and H. F. Meng, Appl. Phys. Lett. **98**, 053305 (2011).

[48] M. K. Ram, O. Yavuz, and M. Aldissi, Synthetic Metals **151**, 77 (2005)

[49] The SCLT characteristics simulation is made based on the device structure shown in Fig. 2. The thicknesses of PVP, Al grid, Al_2O_3, and P3HT are 200, 40, 10, and 400 nm, respectively. The opening diameter is 100 nm. The highest occupied molecular orbital and lowest unoccupied molecular orbital levels of P3HT are 5.2 and 3.0 eV. The work functions of emitter and collector are 5.2 and 4.3 eV. The hole mobility and electron mobility in P3HT are 10^{-5} and 10^{-6} cm^2 /V s.

[50] H. W. Zan, C. H. Li, C. C. Yeh, M. Z. Dai, and H. F. Meng, Appl. Phys. Lett. **98**, 253503 (2011).

[51] K. Wetchakun, T. Samerjai, N. Tamaekong, C. Liewhiran, C. Siriwong, V. Kruefu, A. Wisitsoraat, A. Tuantranont, and S. Phanichphant, Sens. Actuator B **160**, 580 (2011).

[52] C. Wang, H. I Wang, W. T. Tang, C. W. Luo,T. Kobayashi, and J. Leu, Optical Society of America **19**, 24286 (2011).

[53] H. W. Zan, W. W. Tsai, C. H. Chen, and C. C. Tsai, Advanced Materials **23**, 4237 (2011).